

Ill-Posedness Analysis of CSI-Based Electromagnetic Inverse Scattering for Material Reconstruction in ISAC Systems

Yubin Luo, Li Yu, Member, IEEE, Takumi Takahashi, Member, IEEE, Shaoyi Liu, Yuxiang Zhang, Member, IEEE, Jianhua Zhang, Fellow, IEEE, and Hideki Ochiai, Fellow, IEEE

Abstract—Channel state information (CSI)-based electromagnetic inverse scattering for material reconstruction in integrated sensing and communication (ISAC) systems enables physics-grounded, material-aware digital twins (DTs). Yet the resulting CSI-induced scattering operator is often severely ill-conditioned. To understand the origin of the ill-posedness, this paper analyzes the mathematical properties of the electromagnetic inverse problem and investigates the operator structure of the ISAC scattering matrix jointly shaped by in-domain scattering responses and Tx/Rx propagation channels. We show that background-related matrix columns are highly coherent and dominate the near rank deficiency, whereas scatterer-related columns are comparatively weakly correlated; their coherence decreases with the number of probing frequencies and thus contributes to the effective rank. Motivated by this analysis, we prove that restricting the region of interest (ROI) around the true scatterer yields a provable condition-number reduction and a tightened Cramér–Rao lower bound (CRLB), and we quantify the impact of ROI mismatch numerically. To operationalize these insights, an ROI-constrained quadratic programming (QP) framework is adopted, where a linear sampling method delineates a coarse ROI and the QP update is performed in the reduced subspace. Full-wave finite-difference time-domain (FDTD) simulations over multiple geometries and signal-to-noise ratios (SNRs) validate pronounced conditioning improvement, substantial complexity savings, and improved robustness, consistent with the proposed analysis, compared with the full-domain formulation.

Index Terms—Electromagnetic inverse scattering, ill-posedness analysis, material reconstruction, integrated sensing and communication.

I. Introduction

Integrated sensing and communication (ISAC) enables sensing and data transmission on the same waveform, spectrum, and hardware platform [1]. By reusing in-band communication signals and radio frequency (RF) chains, it provides time-synchronized and periodic observations with high spectrum efficiency and low system cost [2], [3], making large-scale online perception and closed-loop

optimization for digital twins (DTs) feasible [4]. A key requirement for such DTs is accurate deterministic channel modeling (e.g., ray tracing and full-wave simulation) to reliably infer channel parameters [5], [6]. Beyond multipath geometry, these models crucially depend on the constitutive parameters of dominant scatterers, which directly govern the electromagnetic channel response. Therefore, constitutive parameter reconstruction (CPR) becomes an essential enabler for DT in sixth generation (6G) wireless communication systems, as it supports deterministic channel modeling while leveraging communication-native measurements.

A variety of CPR methodologies have been investigated in science and engineering. On one end, direct electromagnetic (EM) characterization with specialized instruments (e.g., waveguides and resonators) can achieve high accuracy but typically requires dedicated setups and offline measurements [8]–[10]. On the other end, multimodal and data-driven approaches leverage auxiliary sensing modalities and training data to infer material parameters at scale [11]–[16]. While effective in controlled settings, these approaches are not always compatible with large-scale 6G deployment, where ISAC already provides rich, time-synchronized in-band observations. This motivates a physics-grounded route, namely electromagnetic inverse imaging (EII), which formulates CPR as an inverse scattering problem governed by Maxwell’s equations and integral operators [17]–[19]. In the frequency domain, the wireless multipath channel can be viewed as a parametric surrogate of Green’s-function-based propagation [20]. Therefore, in ISAC systems, our forward model starts from the communication link and treats the resulting channel state information (CSI) as an intrinsic sensing observation. It serves as a surrogate for conventional scattered-field measurements and yields a physics-based mapping from constitutive parameters to the channel observations [21]–[23]. In this work, we focus on the sensing side of ISAC, where the environment is inferred from communication-generated observations, and aim to provide an operator-centric theoretical characterization of ill-posedness under this pilot-aided CSI-driven observation mechanism. Fig. 1 illustrates the considered ISAC-enabled sensing scenario.

ISAC-enabled EII still faces structural limitations, and we highlight two closely related issues. First, DT-oriented deterministic channel modeling demands high-precision

Y. Luo, T. Takahashi and H. Ochiai are with the Graduate School of Engineering, The University of Osaka, 2-1-Yamadaka, Suita, 565-0871, Japan. (e-mail: yubinluo0@gmail.com, takahashi@comm.eng.osaka-u.ac.jp, ochiai@comm.eng.osaka-u.ac.jp.)

L. Yu, S. Liu, Y. Zhang, and J. Zhang are with the State Key Laboratory of Networking and Switching Technology, Beijing University of Posts and Telecommunications, Beijing 100876, China. (e-mail: li.yu@bupt.edu.cn; sy_liu@bupt.edu.cn; zhangyx@bupt.edu.cn; jhzhang@bupt.edu.cn.)

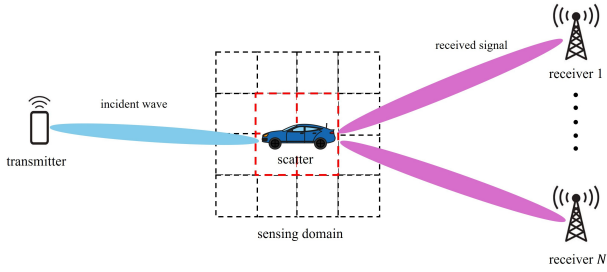


Fig. 1. Schematic diagram of the ISAC system.

CPR, yet inverse-scattering-based CPR is inherently often ill-conditioned. Small singular values of the forward scattering matrix that maps the scene contrast to the measured CSI indicate severe ill-conditioning, leading to high sensitivity to measurement perturbations and pronounced noise amplification [24], [25]. Second, migrating from conventional scattered-field measurements to ISAC-generated CSI fundamentally reshapes the forward model. Unlike classical EII settings, the CSI is jointly shaped by waveform-dependent pilots and the transmitter- and receiver-side propagation channels, resulting in a structured and factorized scattering operator.

The importance of mitigating ill-conditioning has been well recognized under classical scattered-field measurements, and a broad set of techniques—including regularization, multi-frequency, and multi-view strategies—have been developed [12], [13]. Region of interest (ROI) constraints and sampling-based methods have also been employed as practical means to reduce the size of problem space thus enhancing robustness [48]. Nevertheless, it remains unclear how the ISAC-induced scattering operator alters the ill-posedness analysis in CSI-driven CPR, and a unified operator-centric characterization is still limited. In particular, quantitative operator-level studies tailored to ISAC scenarios remain limited. Existing works do not always (i) pinpoint the dominant source of ill-conditioning, (ii) convert the analysis into provable conditioning gains, or (iii) leverage these insights to guide targeted algorithm design that mitigates ill-conditioning in CPR. Moreover, ROI selection is an intrinsic modeling choice and, when mismatched, can affect both reconstruction accuracy and computational complexity.

Motivated by these gaps, we investigate CSI-based CPR in the ISAC systems under a multiple-input multiple-output (MIMO) setting and characterize how the structure of ISAC-induced operator governs the ill-posedness of the associated inverse scattering problem. Our main contributions are as follows:

- We characterize the electromagnetic measurement operator in ISAC systems by revealing its channel-shaped factorization into propagation channels and a scattering-response operator. Building on this structure, we analyze an operator-centric ill-posedness: the systematic ill-conditioning is dominated by highly coherent columns of scattering matrix associated

with the background (air) region, whereas columns corresponding to the actual scatterer region remain comparatively informative due to their weak inter-column coherence, which further decreases with the number of probing frequencies. Based on this analysis, we show that ROI restriction can alleviate ill-posedness by suppressing the redundancy-dominant background subspace.

- We derive rigorous bounds that quantify the reduction in condition-number enabled by the ROI restriction and establish tightened results of Cramér–Rao lower bound (CRLB) within the subspace restricted by ROI, explicitly accounting for the ROI mismatch through precision and recall. These results form a quantitative link from the identified operator analysis to provable conditioning improvements and identifiability gains.
- To operationalize and empirically validate the above operator-level analysis, we use an ROI-restricted quadratic programming (QP) update as a numerical vehicle: the linear sampling method (LSM) yields a coarse support estimate to define the ROI, and the subsequent QP is solved only on the reduced subspace.

The remainder of this paper is organized as follows. Section II introduces the CSI-based forward model and formulates the corresponding CPR problem. Section III provides an operator-centric characterization by revealing the channel-shaped factorization of the forward scattering operator and identifying the dominant mechanisms behind ill-conditioning. Section IV presents an ROI-restricted reconstruction framework to mitigate ill-posedness. Section V quantifies the performance gains of the ROI-restricted formulation in terms of the condition number and the CRLB. Section VI reports numerical results, and Section VII concludes the paper.

Notation: Throughout the paper, boldface symbols denote vectors or matrices; j represents the imaginary unit; $(\cdot)^H$ and $(\cdot)^T$ denote the Hermitian (conjugate transpose) and transpose operations, respectively; $(\cdot)^*$ denotes the complex conjugate of a scalar; $\langle \cdot, \cdot \rangle$ denotes the inner product; $\|\cdot\|_F$ denotes the Frobenius norm; $\|\cdot\|_2$ denotes the Euclidean norm; \circ stands for the Khatri–Rao product; $\text{diag}(\mathbf{x})$ denotes a diagonal matrix whose diagonal entries are formed from the elements of vector \mathbf{x} ; $\mathbf{A}_{[:,i]}$ indicates the i -th column of matrix \mathbf{A} ; \mathbf{I} denotes the identity matrix; $\mathbf{A} \succeq 0$ indicates that matrix \mathbf{A} is positive semi-definite.

II. Basic System Model and Problem Formulation

In this section, we start from a standard baseband channel model and then derive a physics-consistent closed-form expression of the corresponding EM scattering channel from electromagnetic field theory [21]. To reduce the computational complexity of both the forward and inverse problems and to enable efficient repeated solutions, we adopt a two-dimensional transverse magnetic with respect to the z -axis (TM _{z}) with time dependence $e^{j\omega t}$ [31]. Let

$D \subset \mathbb{R}^2$ denote the sensing domain and let Γ denote the observation curve.

Consider a point-to-point MIMO link with an N_t -element Tx array and an N_r -element Rx array. The same input-output formulation also covers a distributed deployment, where N_t (resp. N_r) geographically separated single-antenna transmitters are time/frequency synchronized and jointly form the array; the subsequent derivations depend only on the resulting $N_r \times N_t$ channel matrix at each frequency. Additionally, we assume that all antenna elements are located on an observation curve Γ in the far field of the imaging domain D .

The system operates over K probing frequencies:

$$f_k \triangleq f_c + \left(k - \frac{K+1}{2}\right) \Delta f, \quad k = 1, \dots, K, \quad (1)$$

where f_c and Δf denote the center frequency and the frequency spacing, respectively. At each frequency f_k , the Tx sends T pilot symbols (time slots) to probe the channel. In slot t , a known pilot excitation $\mathbf{x}_{k,t} \in \mathbb{C}^{N_t \times 1}$ produces the received observation $\mathbf{y}_{k,t} \in \mathbb{C}^{N_r \times 1}$ according to:

$$\mathbf{y}_{k,t} = \mathbf{H}_k \mathbf{x}_{k,t} + \mathbf{n}_{k,t}, \quad \mathbf{H}_k \in \mathbb{C}^{N_r \times N_t}, \quad \mathbf{n}_{k,t} \in \mathbb{C}^{N_r \times 1}, \quad (2)$$

where \mathbf{H}_k denotes the end-to-end channel matrix at tone k . Our goal is to express \mathbf{H}_k in closed form as a function of the unknown material contrast, so that inverse-scattering-based CPR can be carried out directly from the pilot-based CSI.

A. End-to-End Scattering Channel

For the k -th frequency (with angular frequency $\omega_k = 2\pi f_k$), the total field inside D satisfies the Lippmann-Schwinger (LS) integral equation [26]–[28]:

$$E_k^t(\mathbf{r}_d) = E_k^i(\mathbf{r}_d) + \int_D G_k(\mathbf{r}_d, \mathbf{r}') \chi(\mathbf{r}'; \omega_k) E_k^t(\mathbf{r}') d\mathbf{r}', \quad (3)$$

where E_k^t and E_k^i denote the total and incident field. \mathbf{r}_d denotes the investigated pixel and \mathbf{r}' is an arbitrary pixel, both on D . $G_k(\mathbf{r}, \mathbf{r}') \triangleq \frac{-j}{4} k_b^2(\omega_k) H_0^{(2)}(k_b(\omega_k) \|\mathbf{r} - \mathbf{r}'\|)$, and $H_0^{(2)}(\cdot)$ denotes the zero-order Hankel function of the second kind with $k_b = \omega_k/c$, c is the speed of light [29], [30]. The contrast is defined as:

$$\chi(\mathbf{r}; \omega_k) \triangleq \varepsilon(\mathbf{r}) - 1 + j \frac{\sigma(\mathbf{r})}{\varepsilon_0 \omega_k}, \quad (4)$$

where $\varepsilon(\mathbf{r})$ is the relative permittivity, $\sigma(\mathbf{r})$ is the conductivity, and ε_0 is the vacuum permittivity and \mathbf{r} is a space point on the two-dimensional Euclidean space. We assume that the material properties vary slowly over the operating band, and thus approximate $\chi(\mathbf{r}; \omega_k) \approx \chi(\mathbf{r}; \omega_c)$ for all k .

By discretizing D into N sampling points, (3) can be written as:

$$\mathbf{E}_k^{t,D} = \mathbf{E}_k^{s,D} + \mathbf{E}_k^{i,D} = \mathbf{E}_k^{i,D} + \mathbf{G}_k^D \text{diag}(\boldsymbol{\chi}) \mathbf{E}_k^{t,D}, \quad (5)$$

where $\mathbf{E}_k^{t,D}, \mathbf{E}_k^{i,D} \in \mathbb{C}^{N \times N_t}$ are the matrices of total and incident fields on D ; $\mathbf{E}_k^{s,D} \in \mathbb{C}^{N \times N_t}$ is the induced scattered field matrix inside D ; $\boldsymbol{\chi} \in \mathbb{C}^{N \times 1}$ is the vector of contrast; and $\mathbf{G}_k^D \in \mathbb{C}^{N \times N}$ is the in-domain Green's matrix.

Let $\mathbf{H}_{1,k}$ and $\mathbf{H}_{2,k}$ denote the propagation channels from the transmitter to D and from D to the receiver array (on Γ), respectively. Then the scattered field on Γ admits the compact end-to-end scattering-channel model:

$$\begin{aligned} \mathbf{E}_{k,t}^{s,\Gamma} &= \mathbf{H}_{2,k} \mathbf{E}_{k,t}^{s,D} \\ &= \mathbf{H}_{2,k} \text{diag}(\boldsymbol{\chi}) \left(\mathbf{I}_N - \mathbf{G}_k^D \text{diag}(\boldsymbol{\chi}) \right)^{-1} \mathbf{H}_{1,k} \mathbf{x}_{k,t}, \end{aligned} \quad (6)$$

where $\mathbf{E}_{k,t}^{s,\Gamma}$ denotes the far-field scattered field after propagation from D through $\mathbf{H}_{2,k}$ [21]. The incident field over D is generated by the transmit excitation through $\mathbf{E}_{k,t}^{i,D} = \mathbf{H}_{1,k} \mathbf{x}_{k,t}$ and $\mathbf{x}_{k,t}$ denotes the pilot signal on f_k and time slot t . In free space, $\mathbf{H}_{1,k} \in \mathbb{C}^{N \times N_t}$ and $\mathbf{H}_{2,k} \in \mathbb{C}^{N_r \times N}$ reduce to the corresponding Green's-function propagation matrices. Throughout this paper, we consider the nominal (coherently calibrated and phase-tracked) propagation operators and generate $\mathbf{H}_{1,k}$ and $\mathbf{H}_{2,k}$ via simulations. This assumption is standard in coherent MIMO imaging, where array calibration is routinely performed to mitigate inter-channel mismatches, and pilot-aided phase-noise tracking is commonly adopted in MIMO receivers [34]–[36].

Following (2) and (6), the received observation at the t -th pilot slot of frequency k is expressed as:

$$\mathbf{y}_{k,t} = \mathbf{H}_{2,k} \text{diag}(\boldsymbol{\chi}) \left(\mathbf{I}_N - \mathbf{G}_k^D \text{diag}(\boldsymbol{\chi}) \right)^{-1} \mathbf{H}_{1,k} \mathbf{x}_{k,t} + \mathbf{n}_{k,t}, \quad (7)$$

where $\mathbf{n}_{k,t}$ denotes receiver noise. Stacking $\{\mathbf{y}_{k,t}\}_{t=1}^T$ and after some simplification [21], the compact form yields:

$$\mathbf{y}_k \triangleq [\mathbf{y}_{k,1}^T, \dots, \mathbf{y}_{k,T}^T]^T = \mathbf{A}_k \boldsymbol{\chi} + \mathbf{n}_k, \quad (8)$$

where $\mathbf{y}_k \in \mathbb{C}^{T N_r \times 1}$, $\mathbf{X}_k \triangleq [\mathbf{x}_{k,1}, \dots, \mathbf{x}_{k,T}] \in \mathbb{C}^{N_t \times T}$ and the forward operator $\mathbf{A}_k \in \mathbb{C}^{T N_r \times N}$ is [21]:

$$\mathbf{A}_k \triangleq \left(\mathbf{X}_k^T \mathbf{H}_{1,k}^T \left[\left(\mathbf{I}_N - \mathbf{G}_k^D \text{diag}(\boldsymbol{\chi}) \right)^{-T} \right] \right) \circ \mathbf{H}_{2,k}. \quad (9)$$

Since \mathbf{A}_k in (9) depends on $\boldsymbol{\chi}$, equation (8) is nonlinear. We adopt the Born iterative method (BIM) to solve (7). At the first iteration, the Born approximation $\mathbf{E}_k^{t,D} \approx \mathbf{E}_k^{i,D}$ yields the linear model

$$\mathbf{y}_k \approx \mathbf{A}_k^{(1)} \boldsymbol{\chi} + \mathbf{n}_k, \quad \mathbf{A}_k^{(1)} = \left(\mathbf{X}_k^T \mathbf{H}_{1,k}^T \right) \circ \mathbf{H}_{2,k}. \quad (10)$$

For iteration $n \geq 2$, $\mathbf{A}_k^{(n)}$ is updated by substituting the previous estimate $\boldsymbol{\chi}^{(n-1)}$ into (9), and $\boldsymbol{\chi}^{(n)}$ is obtained by solving the corresponding linear inverse problem associated with $\mathbf{y}_k \approx \mathbf{A}_k^{(n)} \boldsymbol{\chi} + \mathbf{n}_k$, with the chosen regularization, until convergence [32], [33]. The detailed algorithm will be introduced in Section IV.

B. Linear Sampling Method

To facilitate the subsequent presentation, we briefly recall the linear sampling method [37], which could be used to obtain a coarse geometric support (and hence an ROI) of the scatterer.

For frequency k , the stacked measurement $\mathbf{y}_k \in \mathbb{C}^{T N_r \times 1}$ is calculated by (8). Under the quasi-static assumption within one sensing snapshot, the receive response induced by a unit excitation at the m -th Tx does not depend on the pilot-slot index t . We denote this per-Tx receive stack

by $\mathbf{h}_{k,m} \in \mathbb{C}^{N_r \times 1}$. Then, each $\mathbf{y}_{k,t}$ is the superposition of per-transmit contributions via the known pilot weights:

$$\mathbf{y}_{k,t} = \sum_{m=1}^{N_t} x_{k,t}(m) \mathbf{h}_{k,m} + \mathbf{n}_{k,t}, \quad \mathbf{n}_{k,t} \in \mathbb{C}^{N_r \times 1}, \quad (11)$$

where $x_{k,t}(m)$ is the m -th entry of $\mathbf{x}_{k,t}$.

To match the stacking of \mathbf{y}_k and to exploit T repeated noisy observations for improved robustness, we define the slot-stacked version of $\mathbf{h}_{k,m}$ as

$$\mathbf{h}_{k,m}^{\text{stk}} \triangleq [(\mathbf{h}_{k,m})^T, \dots, (\mathbf{h}_{k,m})^T]^T = \mathbf{1}_T \otimes \mathbf{h}_{k,m} \in \mathbb{C}^{TN_r \times 1}, \quad (12)$$

where $\mathbf{1}_T$ is the all-ones vector of length T and \otimes denotes Kronecker product.

We then form the multi-static response matrix

$$\mathbf{U}_k \triangleq [\mathbf{h}_{k,1}^{\text{stk}}, \dots, \mathbf{h}_{k,N_t}^{\text{stk}}] \in \mathbb{C}^{TN_r \times N_t}, \quad (13)$$

whose m -th column corresponds to the m -th Tx illumination and is stacked in the same way as \mathbf{y}_k .

Typical LSM solves the following linear equation:

$$\mathbf{U}_k \mathbf{c}_k \approx \mathbf{G}_{2,k}^\Gamma, \quad (14)$$

where $\mathbf{c}_k \in \mathbb{C}^{N_t \times N}$ is the LSM coefficient matrix and $\mathbf{G}_{2,k}^\Gamma \in \mathbb{C}^{TN_r \times N}$ denotes the time-slot-stacked scatterer-to-Rx Green's-function propagation matrix. Since the Green's function is time-invariant over the T pilot slots within one snapshot.

In practice, \mathbf{c}_k is obtained via Tikhonov regularization [40]:

$$\mathbf{c}_k = \arg \min_{\mathbf{c}} \|\mathbf{U}_k \mathbf{c} - \mathbf{G}_{2,k}^\Gamma\|_F^2 + \zeta \|\mathbf{c}\|_F^2, \quad (15)$$

where $\zeta > 0$ is the regularization parameter.

After computing $\{\mathbf{c}_k\}_{k=1}^K$, the multi-frequency indicator is formed as [41]

$$\mathcal{J}_K(\mathbf{r}) = \frac{1}{K} \sum_{k=1}^K \log_{10} \left(\|\mathbf{c}_k(\mathbf{r})\|_2^2 \right), \quad (16)$$

where $\mathbf{c}_k(\mathbf{r}) \in \mathbb{C}^{N_t}$ denotes the column of \mathbf{c}_k associated with the test point \mathbf{r} .

In the remaining part of this paper, we focus primarily on the Born-iterative quantitative reconstruction, while the LSM is employed solely for this coarse geometric and ROI initialization.

III. Ill-Posedness Analysis of the ISAC-CSI Operator

A. Operator Structure and Coherence Metric

As discussed in Subsection II-A, the estimation of material contrast from ISAC observations leads to a linear inverse problem of the form (8). In practice, this inverse problem is often severely ill-conditioned, which manifests as pronounced sensitivity to noise and modeling mismatch. A standard quantitative measure of this ill-posedness is the condition number of the forward operator \mathbf{A}_k [42]:

$$\kappa(\mathbf{A}_k) \triangleq \frac{\sigma_{\max}(\mathbf{A}_k)}{\sigma_{\min}(\mathbf{A}_k)}, \quad (17)$$

where $\{\sigma\}$ denote the singular values of \mathbf{A}_k . In the ill-conditioned regime, the rapid decay of $\{\sigma\}$ drives $\sigma_{\min} \approx 0$, rendering \mathbf{A}_k nearly rank-deficient and the inverse problem highly unstable.

A key distinction is that \mathbf{A}_k is channel-shaped: it is formed from CSI extracted from the communication

link rather than from direct scattered-field measurements. Although the formulation ultimately traces back to the Lippmann–Schwinger equation, the intermediate CSI extraction process fundamentally reshapes the forward operator. Specifically, after pilot-assisted CSI extraction with a fixed waveform, the segmented Tx–scatterer–Rx propagation inherent to the wireless channel induces a channelized operator structure, in which each column encodes not only the sensitivity to a local contrast perturbation but is predominantly shaped by propagation and in-domain scattering coupling.

This structure becomes explicit by examining individual columns of \mathbf{A}_k . Let $\mathbf{a}_{k,j}$ denote the j -th column of \mathbf{A}_k . Under the CSI-based observation model, $\mathbf{a}_{k,j}$ takes a Khatri–Rao product form:

$$\mathbf{a}_{k,j} = (\mathbf{A}_k)_{[:,j]} = \mathbf{u}_j \circ \mathbf{v}_j, \quad (18)$$

where

$$\mathbf{u}_j \triangleq \left(\mathbf{X}_k^T \mathbf{H}_{1,k}^T (\mathbf{I} - \mathbf{G}_k^D \text{diag}(\boldsymbol{\chi}))^{-T} \right)_{[:,j]}, \quad (19)$$

$$\mathbf{v}_j \triangleq (\mathbf{H}_{2,k})_{[:,j]}.$$

$\mathbf{u}_j \in \mathbb{C}^{T \times 1}$ is the slot-domain Tx-side signature associated with pixel j after pilot mixing and in-domain coupling, while $\mathbf{v}_j \in \mathbb{C}^{N_r \times 1}$ captures the Rx-side propagation.

From a channel interpretation, \mathbf{u}_j represents the pilot-induced total-field response associated with pixel j , encompassing transmitter-side waveform encoding, Tx-array-to-pixel propagation, and in-domain multiple-scattering coupling. As a result, correlations among $\{\mathbf{u}_j\}$ are jointly shaped by the pilot structure, propagation characteristics, and the contrast distribution. In contrast, $\{\mathbf{v}_j\}$ depends solely on pixel-to-receiver propagation and the receive-array manifold, and therefore admits a simpler, geometry-driven interpretation.

The Khatri–Rao structure in (18) implies that the conditioning properties of \mathbf{A}_k are governed by the joint correlation behavior of $\{\mathbf{u}_j\}$ and $\{\mathbf{v}_j\}$. To quantify this effect, we characterize the inter-column dependence using the normalized cross-correlation (NCC):

$$\mu_{ij} \triangleq \frac{|\langle \mathbf{a}_{k,i}, \mathbf{a}_{k,j} \rangle|}{\|\mathbf{a}_{k,i}\|_2 \|\mathbf{a}_{k,j}\|_2} \in [0, 1], \quad (20)$$

which serves as a direct proxy for column coherence and, consequently, for the degree of ill-conditioning.

In this work, we focus exclusively on the propagation channel induced structure of the ISAC scattering operator, and accordingly fix the pilot configuration throughout the analysis. The impact of pilot design on CPR performance has been studied in [22].

With respect to propagation effects, we adopt a conventional channel model as a neutral baseline. For each probing tone k , the channel is assumed quasi-static within one sensing snapshot and to exhibit approximately stationary spatial statistics over the aperture. Across tones, we allow weak frequency coherence and only assume that the cross-tone correlation is small in a second-order sense. These assumptions aim to capture generic propagation behavior without injecting site-specific structure that could bias the column-correlation analysis. They are

typically reasonable under standard coherence conditions: the quasi-static approximation holds when the snapshot duration is shorter than the channel coherence time, while the inter-tone correlation becomes weak when the tone spacing Δf is comparable to or larger than the coherence bandwidth [38], [39].

Under this controlled setting, we show that the contrast between the background (air) and actual scatterer region (ASR) governs the inter-column correlations of the forward operator and ultimately drives the observed ill-posedness.

B. Air-Region Columns: Strong Coherence

Lemma 1. Columns of \mathbf{A}_k associated with the background (air) region are highly coherent and thus approximately linearly dependent.

Proof. From (19), when the sampling pixel j lies in the background (air) region where the contrast vanishes, the pilot-induced total-field factor \mathbf{u}_j reduces to

$$\mathbf{u}_j = (\mathbf{X}_k^T \mathbf{H}_{1,k}^T)_{[:,j]} = (\mathbf{H}_{1,k} \mathbf{X}_k)_{[:,j]}^T. \quad (21)$$

In this case, the scatterer-induced response vanishes, and \mathbf{u}_j is governed solely by the transmitter-to-pixel propagation channel.

Under the fixed pilot configuration assumed throughout this work, a spatially stationary propagation channel $\mathbf{H}_{1,k}$ induces pronounced correlations among the columns corresponding to nearby background pixels. Furthermore, due to the Khatri–Rao structure $\mathbf{a}_{k,j} = \mathbf{u}_j \circ \mathbf{v}_j$, similar propagation-induced correlations in the pixel-to-receiver channel $\mathbf{H}_{2,k}$ are inherited by the columns of \mathbf{A}_k .

Consequently, in the absence of scatterer-induced interactions, the columns of \mathbf{A}_k associated with the background region predominantly reflect the statistics of the underlying propagation channels. This leads to high mutual coherence and, hence, approximate linear dependence among air-region columns. A rigorous bound on the corresponding column coherence is provided in Appendix B. \square

C. ASR Columns: Weak Coherence

Lemma 2. Columns corresponding to the actual scatterer region are weakly correlated and directly affected by number of probing frequencies.

Proof. Recall $\mathbf{a}_{k,j} = \mathbf{u}_j \circ \mathbf{v}_j$. By (A.1),

$$\mu_{ij} = \frac{|\mathbf{u}_i^H \mathbf{u}_j|}{\|\mathbf{u}_i\|_2 \|\mathbf{u}_j\|_2} \frac{|\mathbf{v}_i^H \mathbf{v}_j|}{\|\mathbf{v}_i\|_2 \|\mathbf{v}_j\|_2}. \quad (22)$$

Within the spatial-coherence regime (Appendix B), there exists $\epsilon_v \in (0, 1)$, which quantifies the maximal deviation of the normalized correlation of the propagation factor \mathbf{v} from unity, such that

$$1 - \epsilon_v \leq \frac{|\mathbf{v}_i^H \mathbf{v}_j|}{\|\mathbf{v}_i\|_2 \|\mathbf{v}_j\|_2} \leq 1. \quad (23)$$

Thus, in the locally coherent propagation regime, the column coherence is dominated by the in-domain factor u_j , whose decorrelation is induced by multiple scattering and multi-frequency phase mixing.

For a homogeneous scatterer, the contrast is spatially constant within the ASR. Let $\mathbf{W} \triangleq \mathbf{X}_k^T \mathbf{H}_{1,k}^T \in \mathbb{C}^{T \times N}$ and $\mathbf{S} \triangleq \mathbf{G}_k^D \text{diag}(\boldsymbol{\chi}) \in \mathbb{C}^{N \times N}$. Then

$$\mathbf{e} \triangleq \mathbf{W}(\mathbf{I} - \mathbf{S})^{-T} \in \mathbb{C}^{T \times N}. \quad (24)$$

Since the scattered-field energy and the number of effective scattering interactions are bounded, spectral radius $\rho(\mathbf{S}) < 1$ holds and the Neumann series converges:

$$\mathbf{e} = \mathbf{W} \sum_{n=0}^{\infty} (\mathbf{S}^T)^n. \quad (25)$$

The zeroth-order term \mathbf{W} corresponds to propagation without contrast-induced coupling, while the higher-order terms represent in-domain multiple scattering. The additional decorrelation inside the ASR is therefore governed by the in-domain Green's function \mathbf{G}_k^D .

Let $\mathbf{G}_{k,\text{ASR}}^D \in \mathbb{C}^{N_d \times N_d}$ denote the in-domain Green's submatrix restricted to the ASR grid with N_d pixels, and let $\mathbf{g}_{k,i} \triangleq [\mathbf{G}_{k,\text{ASR}}^D]_{[:,i]} \in \mathbb{C}^{N_d \times 1}$. Using the large-argument expansion of the Hankel function, the inner product between two distinct columns can be written as:

$$\mathbf{g}_{k,i}^H \mathbf{g}_{k,j} = \sum_{m=1}^{N_d} \alpha_{m,k} \exp(-j\phi_{ij,k}(\mathbf{r}_m)) + \Delta_{k,ij}, \quad (26)$$

where

$$\phi_{ij,k}(\mathbf{r}_m) \triangleq k_b \left(\|\mathbf{r}_m - \mathbf{r}_j\|_2 - \|\mathbf{r}_m - \mathbf{r}_i\|_2 \right), \quad (27)$$

and k_b denotes the background wavenumber at tone k . Define $d_{m,i} \triangleq \|\mathbf{r}_m - \mathbf{r}_i\|_2$ and $d_{m,j} \triangleq \|\mathbf{r}_m - \mathbf{r}_j\|_2$. The amplitude weight induced by the large-argument Hankel expansion is

$$\alpha_{m,k} \triangleq \frac{2|b_k|^2}{\pi k_b \sqrt{d_{m,i} d_{m,j}}}, \quad b_k \triangleq -\frac{j}{4} k_b^2. \quad (28)$$

This approximation is valid when $k_b d \gg 1$, a condition that typically holds in the 28 GHz band.

The remainder term $\Delta_{k,ij}$ collects the higher-order terms ignored in the Hankel asymptotic:

$$\Delta_{k,ij} \triangleq \sum_{m=1}^{N_d} \left(G_k(\mathbf{r}_m, \mathbf{r}_i)^* G_k(\mathbf{r}_m, \mathbf{r}_j) - \alpha_{m,k} e^{-j\phi_{ij,k}(\mathbf{r}_m)} \right). \quad (29)$$

Define the geometry-induced effective phase

$$\varphi_{ij,k} \triangleq \arg \left(\sum_{m=1}^{N_d} \alpha_{m,k} e^{-j\phi_{ij,k}(\mathbf{r}_m)} \right). \quad (30)$$

Across frequencies, we characterize the multi-frequency phase-mixing effect under the standard frequency-incoherent regime, where the tone spacing Δf exceeds the coherence bandwidth so that cross-tone correlations are weak. We model the aggregate residual by an i.i.d. random phase $\theta_k \sim \text{Unif}[0, 2\pi)$ across tones, independent of the geometry, and define the cross-tone phasor as:

$$z_k(i, j) \triangleq \exp(j(\varphi_{ij,k} + \theta_k)), \quad \bar{z}(i, j) \triangleq \frac{1}{K} \sum_{k=1}^K z_k(i, j). \quad (31)$$

In the frequency-incoherent regime, cross-tone correlations are weak. We formalize this at the second-order level by

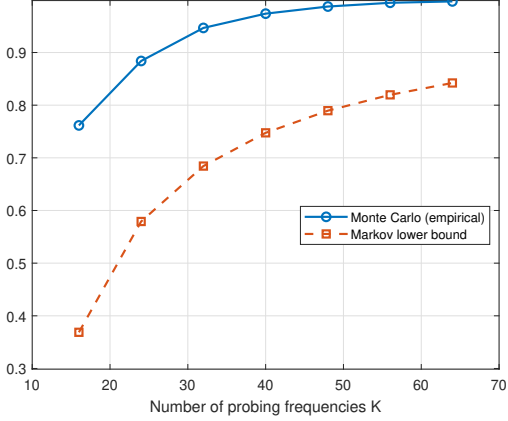


Fig. 2. Probability of Low Residual Coherence versus K .

assuming

$$\begin{aligned} |z_k(i, j)| &= 1, \\ \mathbb{E}[z_k(i, j)] &= 0, \\ \mathbb{E}[z_k(i, j) z_\ell(i, j)^*] &= 0, \quad \forall k \neq \ell. \end{aligned} \quad (32)$$

Under (32), we further derive

$$\begin{aligned} \mathbb{E}[|\bar{z}(i, j)|^2] &= \mathbb{E}\left[\left|\frac{1}{K} \sum_{k=1}^K z_k(i, j)\right|^2\right] \\ &= \frac{1}{K^2} \mathbb{E}\left[\sum_{k=1}^K \sum_{\ell=1}^K z_k(i, j) z_\ell(i, j)^*\right] \\ &= \frac{1}{K^2} \left(\sum_{k=1}^K \mathbb{E}[|z_k(i, j)|^2] + \sum_{k \neq \ell} \mathbb{E}[z_k(i, j) z_\ell(i, j)^*] \right) \\ &= \frac{1}{K^2} (K \cdot 1 + 0) = \frac{1}{K}. \end{aligned} \quad (33)$$

Fix a target failure probability $\delta \in (0, 1)$. Applying Markov's inequality to $|\bar{z}(i, j)|^2$ yields

$$\mathbb{P}\left(\left|\frac{1}{K} \sum_{k=1}^K \exp(j(\varphi_{ij,k} + \theta_k))\right| \leq \sqrt{\frac{1}{K\delta}}\right) \geq 1 - \delta. \quad (34)$$

The above inequality indicates that, for any two distinct locations ($i \neq j$), the multi-frequency phasor average concentrates near zero with probability at least $1 - \delta$, leading to weak inter-column correlation. Moreover, the residual coherence decreases with the number of probing tones K : larger K yields stronger phase mixing and a higher chance that the coherence stays below a prescribed level. Therefore, with a proper choice of K , the columns associated with the ASR are weakly correlated with high probability and remain informative in the effective sensing operator. This aligns with the empirical observation that multi-frequency sensing leads to improved CPR performance.

To further illustrate this dependence on the probing frequency number, Fig. 2 presents a numerical verification based on the phase-randomization model. The horizontal axis corresponds to the number of probing frequencies, while the vertical axis reports the success probability that

the residual coherence between two ASR-related columns stays below a fixed threshold, which is set to 0.25. The blue curve represents the Monte Carlo empirical probability, which closely reflects the actual behavior under the adopted statistical model, whereas the orange curve shows a conservative analytical lower bound obtained from the second-moment analysis via the Markov inequality. As the number of probing frequencies increases, both curves exhibit a pronounced upward trend, confirming that multi-frequency averaging effectively suppresses residual coherence and drives the inter-column correlation toward the weakly correlated regime. \square

Consequently, these observations imply that once the frequency-dimension diversity is fixed by system constraints, the spatial selection of the ROI becomes the predominant factor in governing the problem's ill-posedness. In this regime, the system's conditioning is highly dictated by the inclusion of strong coherent background columns, underscoring ROI restriction as the decisive mechanism for stabilizing the material reconstruction process.

IV. Empirical Validation via ROI-Constrained Subproblems

A. ROI-Constrained Quadratic-Programming

To examine how the coherence behavior characterized in Section III manifests in practice, this section provides an implementation example for empirical validation under ISAC constraints. Consistent with the theoretical bounds in Section III, the core objective is to restrict the inversion within an ROI that matches the ASR, thereby suppressing the ill-conditioned background-related subspace and stabilizing the reconstruction.

From a system perspective, ISAC platforms operate under a paradigm fundamentally different from dedicated laboratory imaging. Sensing functionalities must coexist with high-rate communication services, demanding that environmental perception be achieved within stringent latency budgets and limited on-board computational resources. Consequently, the acquisition of geometric priors for ROI delineation must be low-overhead and real-time capable, avoiding the heavy iterations typical of full-domain quantitative inversion.

Driven by these ISAC-specific constraints, we employ the LSM as a lightweight geometric pre-processing tool. Rather than being a mere algorithmic choice, LSM is selected for its ability to rapidly extract the scatterer support from the CSI through simple linear operations, providing a coarse yet effective geometric prior at a fraction of the cost of iterative solvers [38]. This ensures that the sensing-communication trade-off is maintained by offloading the complexity of "where to look" to a fast qualitative step, while reserving computational power for the "what it is" quantitative refinement in the reduced subspace.

In particular, we compute the multi-frequency LSM indicator from the multi-static response matrix \mathbf{U}_k (see

Algorithm 1: Trimmed max-gap thresholding for ROI selection

Input: $\{\mathbf{U}_k\}_{k=1}^K$, $\epsilon > 0$, $q_{\text{trim}} \in (0, \frac{1}{2}]$.
Output: $\eta > 0$.

- 1 Compute the multi-frequency LSM indicator $\mathcal{J}_K \in \mathbb{R}^N$ via (15)–(16).
- 2 Normalize scores: $s_p \leftarrow \frac{\mathcal{J}_{K,\text{max}} - [\mathcal{J}_K]_p}{\mathcal{J}_{K,\text{max}} - \mathcal{J}_{K,\text{min}} + \epsilon}$, $\forall p$.
- 3 Sort $\{s_p\}$ increasingly to obtain $\{s_{(i)}\}_{i=1}^N$ and gaps $\Delta_i \leftarrow s_{(i+1)} - s_{(i)}$.
- 4 $w \leftarrow \lceil q_{\text{trim}} N \rceil$; $i^* \in \arg \max_{i \in \{w, \dots, N-1-w\}} \Delta_i$;
 $\eta \leftarrow \frac{1}{2}(s_{(i^*)} + s_{(i^*+1)})$.
- 5 return η .

subsection II-B) and delineate the ROI by an automatic, data-driven threshold. Specifically, we normalize the indicator values and determine the threshold η via a trimmed maximum-gap rule on the sorted scores: after trimming both tails to suppress outliers, we select η as the midpoint of the largest adjacent gap, which serves as a separator between background-like and scatterer-like pixels. The stabilizer ϵ is introduced only to avoid numerical degeneracy in the normalization.

The overall procedure is summarized in Algorithm 1.

So far, the ROI index set can be defined as

$$\mathcal{I} \triangleq \{p : s_p \leq \eta\}, \quad (35)$$

with size $P \triangleq |\mathcal{I}|$, where s_p computed in Algorithm 1 denotes an error-like score, with smaller values indicating more scatterer-like pixels.

Because the max-gap rule is invariant to any positive affine rescaling of \mathcal{J}_K , the stabilizer ϵ serves only to prevent a near-zero denominator and does not affect the threshold or ROI. Similarly, q_{trim} merely trims values and, within a reasonable range, does not change the position of the maximal gap; hence, its impact on the thresholding outcome is negligible.

Using the ROI indices, we form the submatrix:

$$\mathbf{A}_k^{\text{sub}} \triangleq [\mathbf{A}_k]_{[:, \mathcal{I}]} \in \mathbb{C}^{TN_r \times P}, \quad (36)$$

where $P \ll N$ is the size of \mathcal{I} . Next, the received signals \mathbf{y}_k and the corresponding submatrices $\mathbf{A}_k^{\text{sub}}$ for $k = 1, \dots, K$ are stacked vertically according to their frequency index, forming the vector \mathbf{Y} and matrix \mathbf{A}^{sub} , as follows:

$$\mathbf{Y} \triangleq \begin{bmatrix} \mathbf{y}_1 \\ \mathbf{y}_2 \\ \vdots \\ \mathbf{y}_K \end{bmatrix}, \quad \mathbf{A}^{\text{sub}} \triangleq \begin{bmatrix} \mathbf{A}_1^{\text{sub}} \\ \mathbf{A}_2^{\text{sub}} \\ \vdots \\ \mathbf{A}_K^{\text{sub}} \end{bmatrix}. \quad (37)$$

where $\mathbf{Y} \in \mathbb{C}^{KTN_r \times 1}$ and $\mathbf{A}^{\text{sub}} \in \mathbb{C}^{KTN_r \times P}$.

Let $\boldsymbol{\chi}^{\text{sub}} \triangleq \boldsymbol{\chi}_{\mathcal{I}}$ denote the subset of the contrast vector restricted to the ROI. By solving the frequency-stacked subproblem:

$$\mathbf{Y} = \mathbf{A}^{\text{sub}} \boldsymbol{\chi}^{\text{sub}} + \mathbf{d}, \quad \mathbf{d} \in \mathbb{C}^{KTN_r \times 1}, \quad (38)$$

where \mathbf{d} denotes the residuals between real observations and equivalent predictions. This linear system is solved via a convex QP formulation [43]. Since both the measurements and unknowns are complex-valued, we convert

Algorithm 2: ROI-Constrained Quadratic Programming (ROI-QP)

Input: $\{\mathbf{y}_k\}_{k=1}^K$, η , (l, s, α, β) , (τ_{err}, M) .
Output: $\hat{\boldsymbol{\chi}}$.

- 1 Let $\Omega \triangleq \{1, 2, \dots, N\}$ denote the full index set of the discretized domain.
- 2 Compute ROI index set: Obtain $\mathcal{I} \subseteq \Omega$ from η via (35). // ROI delineation motivated by Lemma 2
- 3 Initialization:
- 4 $n \leftarrow 1$; $\boldsymbol{\chi}^{(1)} \leftarrow \mathbf{0}$; $\boldsymbol{\chi}^{\text{sub}(1)} \leftarrow \mathbf{0}$; $\Delta \leftarrow +\infty$.
- 5 $\mathbf{Y} \leftarrow [\mathbf{y}_1; \dots; \mathbf{y}_K]$.
- 6 foreach $k \in \{1, \dots, K\}$ do
- 7 $\mathbf{A}_k^{(1)} \leftarrow (\mathbf{X}_k^T \mathbf{H}_{1,k}^T) \circ \mathbf{H}_{2,k}$.
- 8 while $\Delta > \tau_{\text{err}}$ and $n < M$ do
- 9 Updating $\mathbf{A}_k^{(n)}$ by (9) ($n \geq 2$).
- 10 $\mathbf{A}^{\text{sub}(n)} \leftarrow [\mathbf{A}_1^{(n)}[:, \mathcal{I}]; \dots; \mathbf{A}_K^{(n)}[:, \mathcal{I}]]$. // guided by Lemma 1
- 11 Obtain $(\tilde{\mathbf{A}}^{\text{sub}(n)}, \tilde{\mathbf{Y}})$ by applying the real-valued reformulation in (39) to $(\mathbf{A}^{\text{sub}(n)}, \mathbf{Y})$.
- 12 $\mathbf{L}_R \leftarrow \text{Laplacian}(\mathcal{I})$.
- 13 QP-Assemble: construct $(\mathbf{M}, \mathbf{R}, \mathbf{l}', \mathbf{s}')$ from $(\tilde{\mathbf{A}}^{\text{sub}(n)}, \mathbf{L}_R, \tilde{\mathbf{l}}, \tilde{\mathbf{s}}, \alpha, \beta)$ according to (42).
- 14 QP-Solve: $\tilde{\boldsymbol{\chi}}^{\text{sub}(n)} \leftarrow (\mathbf{M}, \mathbf{R}, \tilde{\mathbf{Y}}, \mathbf{l}', \mathbf{s}')$ via (43).
// Optimization within the stabilized ROI
- 15 $\boldsymbol{\chi}^{\text{sub}(n)} \leftarrow \tilde{\boldsymbol{\chi}}_{1:P}^{\text{sub}(n)} + j \tilde{\boldsymbol{\chi}}_{P+1:2P}^{\text{sub}(n)}$.
- 16 $\boldsymbol{\chi}^{(n)}[\mathcal{I}] \leftarrow \boldsymbol{\chi}^{\text{sub}(n)}$; $\boldsymbol{\chi}^{(n)}[\Omega \setminus \mathcal{I}] \leftarrow 0$.
// Background nulling to suppress coherence
- 17 $\Delta \leftarrow \|\boldsymbol{\chi}^{\text{sub}(n)} - \boldsymbol{\chi}^{\text{sub}(n-1)}\|_2$; $n \leftarrow n + 1$.
- 18 return $\hat{\boldsymbol{\chi}} \leftarrow \boldsymbol{\chi}^{(n)}$.

the complex system into an equivalent real-valued form that can be handled by standard QP solvers. We define the real-valued representation:

$$\tilde{\boldsymbol{\chi}}^{\text{sub}} \triangleq \begin{bmatrix} \Re\{\boldsymbol{\chi}^{\text{sub}}\} \\ \Im\{\boldsymbol{\chi}^{\text{sub}}\} \end{bmatrix}, \quad \tilde{\mathbf{d}} \triangleq \begin{bmatrix} \Re\{\mathbf{d}\} \\ \Im\{\mathbf{d}\} \end{bmatrix}, \quad \tilde{\mathbf{Y}} \triangleq \begin{bmatrix} \Re\{\mathbf{Y}\} \\ \Im\{\mathbf{Y}\} \end{bmatrix},$$

$$\tilde{\mathbf{A}}^{\text{sub}} \triangleq \begin{bmatrix} \Re\{\mathbf{A}^{\text{sub}}\} & -\Im\{\mathbf{A}^{\text{sub}}\} \\ \Im\{\mathbf{A}^{\text{sub}}\} & \Re\{\mathbf{A}^{\text{sub}}\} \end{bmatrix}. \quad (39)$$

Then $\tilde{\boldsymbol{\chi}}^{\text{sub}} \in \mathbb{R}^{2P \times 1}$, $\tilde{\mathbf{Y}}, \tilde{\mathbf{d}} \in \mathbb{R}^{2KTN_r \times 1}$, and $\tilde{\mathbf{A}}^{\text{sub}} \in \mathbb{R}^{2KTN_r \times 2P}$.

The complex equality constraint $\mathbf{A}^{\text{sub}} \boldsymbol{\chi}^{\text{sub}} - \mathbf{Y} + \mathbf{d} = 0$ is equivalently written as $\tilde{\mathbf{A}}^{\text{sub}} \tilde{\boldsymbol{\chi}}^{\text{sub}} - \tilde{\mathbf{Y}} + \tilde{\mathbf{d}} = 0$.

We solve the following convex QP:

$$\begin{aligned} \min_{\tilde{\boldsymbol{\chi}}^{\text{sub}}, \tilde{\mathbf{d}}} \quad & \frac{1}{2} \|\tilde{\mathbf{d}}\|_2^2 + \frac{\alpha}{2} \|\tilde{\boldsymbol{\chi}}^{\text{sub}}\|_2^2 + \frac{\beta}{2} (\tilde{\boldsymbol{\chi}}^{\text{sub}})^T \text{blkdiag}(\mathbf{L}_R, \mathbf{L}_R) \tilde{\boldsymbol{\chi}}^{\text{sub}}, \\ \text{s.t.} \quad & \tilde{\mathbf{A}}^{\text{sub}} \tilde{\boldsymbol{\chi}}^{\text{sub}} - \tilde{\mathbf{Y}} + \tilde{\mathbf{d}} = 0, \\ & \tilde{\mathbf{l}} \leq \tilde{\boldsymbol{\chi}}^{\text{sub}} \leq \tilde{\mathbf{s}}. \end{aligned} \quad (40)$$

where $\text{blkdiag}(\cdot)$ denotes the block-diagonal concatenation of the corresponding matrices. $\alpha \geq 0$ and $\beta \geq 0$ weight the standard Tikhonov regularization and the ROI graph-Laplacian smoothness, respectively. The box constraints $\tilde{\mathbf{l}}, \tilde{\mathbf{s}}$ simply enforce element-wise bounds on $\tilde{\boldsymbol{\chi}}^{\text{sub}}$. In this

paper they are chosen sufficiently loose so that they do not affect the final reconstruction results.

The ROI graph Laplacian is defined as [44]

$$\mathbf{L}_R = \mathbf{Q} - \mathbf{B}, \quad (41)$$

where \mathbf{Q} and \mathbf{B} denote the degree and adjacency matrices, respectively. \mathbf{B} is constructed using 4-nearest-neighbor connectivity on the ROI grid with unit weights.

Define

$$\begin{aligned} \mathbf{z} &\triangleq \begin{bmatrix} \tilde{\boldsymbol{\chi}}^{\text{sub}} \\ \tilde{\mathbf{d}} \end{bmatrix} \in \mathbb{R}^{(2P+2KT_N_r) \times 1}, \\ \mathbf{M} &\triangleq \begin{bmatrix} \alpha \mathbf{I}_{2P} + \beta \text{blkdiag}(\mathbf{L}_R, \mathbf{L}_R) & \mathbf{0} \\ \mathbf{0} & \mathbf{I}_{2KT_N_r} \end{bmatrix}, \\ \mathbf{R} &\triangleq [\tilde{\mathbf{A}}^{\text{sub}} \quad \mathbf{I}_{2KT_N_r}]. \end{aligned} \quad (42)$$

Accordingly, (40) can be written as

$$\min_{\mathbf{z}} \frac{1}{2} \mathbf{z}^T \mathbf{M} \mathbf{z} \quad \text{s.t.} \quad \mathbf{R} \mathbf{z} = \tilde{\mathbf{Y}}, \quad \mathbf{l}' \leq \mathbf{z} \leq \mathbf{s}', \quad (43)$$

where \mathbf{l}' and \mathbf{s}' are obtained by padding $\tilde{\mathbf{l}}$ and $\tilde{\mathbf{s}}$ with $-\infty$ and $+\infty$ entries of length $2KT_N_r$.

Assuming convergence after M iterations, the reconstructed $\boldsymbol{\chi}^{\text{sub}}$ is extended to the full contrast vector $\boldsymbol{\chi}$ by assigning zero contrast to entries outside the ROI. The complete workflow is summarized in Algorithm 2.

B. Analysis of Algorithm Complexity

Using the ROI prior to constrain the QP within a subspace of D not only alleviates the ill-posedness of the linear equations but also significantly reduces the problem size, leading to substantial gains in computational efficiency. The computational complexity of the LSM is dominated by solving (15) over all N test points for each tone scaling as $O(K(N_t^3 + TNN_rN_t))$. For each outer iteration, the complexity of constructing the ROI-restricted operators $\{\mathbf{A}_k^{\text{sub}}\}_{k=1}^K$ (using (9) on the ROI grid) and stacking them according to (37) is $O(K(P^3 + TN_tP + TP^2 + 2TN_rP))$. The complexity of solving the convex QP problem (43) is upper-bounded by $O(P^3 + P^2 + 2KT_N_rP)$. After systematic organization using Big- O notation, the overall computational complexity of the algorithm becomes $O(MK(P^3 + TP^2 + T(N_t + N_r)P) + K(N_t^3 + TNN_rN_t))$. It can be observed that, when using ROI-restricted solving with a pixel count $P \ll N$, the computational complexity is significantly reduced.

V. Performance Analysis of ROI-Constrained QP Optimization

A. Condition Number Reduction via ROI Constraint

Because estimation errors may arise in the LSM output, the resulting ROI may not perfectly coincide with the true ASR, leading to either partial exclusion of ASR pixels or inclusion of background (air) pixels. In this subsection, we analyze such ROI mismatches and show that, despite these imperfections, the ROI-constrained QP formulation still admits a tighter upper bound on the condition number $\kappa(\mathbf{A}^{\text{sub}})$ than the unconstrained formulation.

For analytical clarity, we focus on the single-frequency case. We present the derivation for a fixed tone k with $\mathbf{A}^{\text{sub}} = \mathbf{A}_k^{\text{sub}} \in \mathbb{C}^{TN_r \times P}$, and the multi-frequency case follows by replacing \mathbf{A}^{sub} with the stacked operator in (37). Since the multi-frequency setting corresponds to a row-wise stacking of per-frequency measurements, the resulting condition-number behavior directly extends to the multi-frequency scenario.

Let the set of all pixels be $\Omega \triangleq \{1, \dots, N\}$. The set of ASR pixels is denoted by $S_{\text{true}} \subset \Omega$ with cardinality $k_{\text{true}} \triangleq |S_{\text{true}}|$.

Let $\mathcal{I} \subset \Omega$ denote the ROI index set with $P \triangleq |\mathcal{I}|$. The ROI can be decomposed into true positives and false positives as

$$\begin{aligned} \mathcal{T} &\triangleq \mathcal{I} \cap S_{\text{true}}, \quad \tau \triangleq |\mathcal{T}|, \\ \mathcal{F} &\triangleq \mathcal{I} \setminus S_{\text{true}}, \quad n_{\text{fp}} \triangleq |\mathcal{F}| = P - \tau. \end{aligned} \quad (44)$$

Accordingly, we define the recall \mathcal{R} and the precision p_{prec} as

$$\mathcal{R} \triangleq \frac{\tau}{k_{\text{true}}}, \quad p_{\text{prec}} \triangleq \frac{\tau}{P} = \frac{\tau}{\tau + n_{\text{fp}}}. \quad (45)$$

Next, define the normalized Gram matrix of the ROI sub-operator as

$$\boldsymbol{\Phi}_{\mathcal{I}} \triangleq (\bar{\mathbf{A}}^{\text{sub}})^H (\bar{\mathbf{A}}^{\text{sub}}), \quad (46)$$

where $\bar{\mathbf{A}}^{\text{sub}}$ represents the normalized version of \mathbf{A}^{sub} ; $[\boldsymbol{\Phi}_{\mathcal{I}}]_{jj} = 1$ for all $j \in \mathcal{I}$, and each off-diagonal entry equals the NCC between the corresponding two ROI columns. Let $\bar{\mathbf{A}}^{\text{sub}} \triangleq \mathbf{A}^{\text{sub}} \mathbf{D}^{-1}$, where $\mathbf{D} \triangleq \text{diag}(\|\mathbf{a}_1\|_2, \dots, \|\mathbf{a}_P\|_2) \in \mathbb{R}^{P \times P}$, so that each column of $\bar{\mathbf{A}}^{\text{sub}} \in \mathbb{C}^{TN_r \times P}$ has unit ℓ_2 norm.

We further define:

$$\mu_{\text{eff}} \triangleq \max_{j \neq p} |[\boldsymbol{\Phi}_{\mathcal{I}}]_{jp}|, \quad (47)$$

which represents the largest off-diagonal magnitude of $\boldsymbol{\Phi}_{\mathcal{I}}$ and thus upper-bounds the pairwise NCC among ROI columns. In addition, for any $j \in \mathcal{I}$, we define

$$R_j \triangleq \sum_{p \neq j} |[\boldsymbol{\Phi}_{\mathcal{I}}]_{jp}| \leq (P-1) \mu_{\text{eff}}, \quad (48)$$

where R_j denotes the Gershgorin radius, obtained by using μ_{eff} as a uniform bound [47]. For notational simplicity, we re-index the ROI columns from 1 to P . By the Gershgorin disk theorem, the spectrum of $\boldsymbol{\Phi}_{\mathcal{I}}$ is contained within the union of disks:

$$\begin{aligned} \sigma(\boldsymbol{\Phi}_{\mathcal{I}}) &\subset \bigcup_{j=1}^P \left\{ z \in \mathbb{C} : |z - [\boldsymbol{\Phi}_{\mathcal{I}}]_{jj}| \leq R_j \right\}, \\ &= \bigcup_{j=1}^P \left\{ z \in \mathbb{C} : |z - 1| \leq R_j \right\}. \end{aligned} \quad (49)$$

Since $\boldsymbol{\Phi}_{\mathcal{I}}$ is Hermitian, its spectrum satisfies $\sigma(\boldsymbol{\Phi}_{\mathcal{I}}) \subset \mathbb{R}$, i.e.,

$$1 - R_{\text{max}} \leq \lambda_{\min}(\boldsymbol{\Phi}_{\mathcal{I}}) \leq \lambda_{\max}(\boldsymbol{\Phi}_{\mathcal{I}}) \leq 1 + R_{\text{max}}, \quad (50)$$

where $R_{\text{max}} \triangleq \max_j R_j$. λ_{\min} and λ_{\max} denote the minimum and maximum eigenvalues of $\boldsymbol{\Phi}_{\mathcal{I}}$, respectively.

Finally, we introduce the following condition solely to obtain a finite and explicit closed-form bound through the Gershgorin argument; it should be viewed as a sufficient condition:

$$(P-1) \mu_{\text{eff}} < 1. \quad (51)$$

Under this condition, $1 - R_{\max} > 0$ and hence $\lambda_{\min}(\Phi_{\mathcal{I}}) > 0$, ensuring that the derived bound is well-defined. More broadly, the bound is used as a conservative analytic certificate to reveal how the effective coherence μ_{eff} and the leakage factor R_{\max} shape the conditioning of the ROI-restricted subspace. When the above inequality is not satisfied (e.g., for moderately large P), the closed-form value may be less tight, and we therefore rely on the exact spectral quantity (or numerical evaluation) to quantify the conditioning, while the monotonic trend with respect to μ_{eff} and R_{\max} remains consistent.

Under the above sufficient condition we obtain:

$$\begin{aligned} \kappa(\bar{\mathbf{A}}^{\text{sub}}) &\leq \sqrt{\frac{1 + R_{\max}}{1 - R_{\max}}} \leq \sqrt{\frac{1 + (P-1)\mu_{\text{eff}}}{1 - (P-1)\mu_{\text{eff}}}}, \\ &= \sqrt{\frac{1 + \left(\frac{\mathcal{R}}{p_{\text{prec}}} k_{\text{true}} - 1\right) \mu_{\text{eff}}}{1 - \left(\frac{\mathcal{R}}{p_{\text{prec}}} k_{\text{true}} - 1\right) \mu_{\text{eff}}}}. \end{aligned} \quad (52)$$

All bounds above apply to the column-normalized ROI operator at the considered tone.

Next, define $\xi \triangleq \left(\frac{\mathcal{R}}{p_{\text{prec}}} k_{\text{true}} - 1\right) \mu_{\text{eff}}$, and $\kappa_{\max} \triangleq \sqrt{\frac{1+\xi}{1-\xi}}$ as the maximum $\kappa(\mathbf{A}^{\text{sub}})$. Thus, we derive the following calculations:

$$\begin{aligned} \frac{\partial \ln \kappa_{\max}}{\partial \xi} &= \frac{1}{2} \left(\frac{1}{1+\xi} + \frac{1}{1-\xi} \right) \\ &= \frac{1}{1-\xi^2}; \\ \frac{\partial \ln \kappa_{\max}}{\partial \mu_{\text{eff}}} &= \frac{\partial \ln \kappa_{\max}}{\partial \xi} \cdot \frac{\partial \xi}{\partial \mu_{\text{eff}}} \\ &= \frac{1}{1-\xi^2} \left(\frac{\mathcal{R}}{p_{\text{prec}}} k_{\text{true}} - 1 \right) \\ &= \frac{P-1}{1-\xi^2}, \end{aligned} \quad (53)$$

and therefore,

$$\frac{\partial \ln \kappa_{\max}}{\partial \mu_{\text{eff}}} \frac{\partial \mu_{\text{eff}}}{\partial \ln \kappa_{\max}} = P-1. \quad (54)$$

This analysis indicates that the variation of the condition number κ is primarily governed by μ_{eff} . When the ROI is moderately large, this dependence is more pronounced. In light of Section II, even if a small number of air-region columns remain within the ROI, the columns in the ROI remain weakly correlated as long as the ASR columns dominate. Consequently, the effective coherence μ_{eff} is substantially smaller than that of the full sensing region, leading to a correspondingly tighter and smaller upper bound on κ . We adopt the column-normalized operator $\bar{\mathbf{A}}^{\text{sub}}$ to isolate the correlation mechanism; the ROI-induced reduction of inter-column coherence is the key driver of conditioning improvement for \mathbf{A}^{sub} .

B. Analysis of the Cramér–Rao Lower Bound

Consider the ROI-restricted linear model

$$\mathbf{y} = \mathbf{A}^{\text{sub}} \boldsymbol{\chi}^{\text{sub}} + \mathbf{n}, \quad \mathbf{n} \sim \mathcal{CN}(\mathbf{0}, \sigma_n^2 \mathbf{I}), \quad (55)$$

where $\boldsymbol{\chi}^{\text{sub}} \in \mathbb{C}^{P \times 1}$, $\mathbf{y} \in \mathbb{C}^{TN_r \times 1}$, $\mathbf{A}^{\text{sub}} \in \mathbb{C}^{TN_r \times P}$ and σ_n^2 denotes the noise variance.

For the proper-complex Gaussian model in (55), the CRLB for any unbiased estimator $\hat{\boldsymbol{\chi}}^{\text{sub}}$ can be written in the compact complex form:

$$\text{Cov}(\hat{\boldsymbol{\chi}}^{\text{sub}}) \succeq \sigma_n^2 ((\mathbf{A}^{\text{sub}})^{\text{H}} \mathbf{A}^{\text{sub}})^{-1}. \quad (56)$$

Let $\mathcal{Z} \triangleq (\mathbf{A}^{\text{sub}})^{\text{H}} \mathbf{A}^{\text{sub}}$. Then

$$\begin{aligned} \lambda_{\max}(\text{Cov}(\hat{\boldsymbol{\chi}}^{\text{sub}})) &\geq \sigma_n^2 \lambda_{\max}(\mathcal{Z}^{-1}) \\ &= \frac{\sigma_n^2}{\lambda_{\min}(\mathcal{Z})} = \frac{\sigma_n^2}{\sigma_{\min}^2(\mathbf{A}^{\text{sub}})}. \end{aligned} \quad (57)$$

To connect (57) to the correlation mechanism, define the column-normalized matrix $\bar{\mathbf{A}}^{\text{sub}} \triangleq \mathbf{A}^{\text{sub}} \mathbf{D}^{-1}$ with

$$\mathbf{D} \triangleq \text{diag}(\|\mathbf{a}_1\|_2, \dots, \|\mathbf{a}_P\|_2), \quad (58)$$

where $\{\mathbf{a}_i\}_{i=1}^P$ are the columns of \mathbf{A}^{sub} , so that $\|\bar{\mathbf{a}}_i\|_2 = 1$. Let μ_{eff} denote the effective mutual coherence of $\bar{\mathbf{A}}^{\text{sub}}$:

$$\mu_{\text{eff}} \triangleq \max_{i \neq j} |\bar{\mathbf{a}}_i^{\text{H}} \bar{\mathbf{a}}_j|. \quad (59)$$

By Gershgorin's theorem, if $1 - (P-1)\mu_{\text{eff}} > 0$, then

$$\lambda_{\min}((\bar{\mathbf{A}}^{\text{sub}})^{\text{H}} \bar{\mathbf{A}}^{\text{sub}}) \geq 1 - (P-1)\mu_{\text{eff}}. \quad (60)$$

Next, note that $\mathbf{A}^{\text{sub}} = \bar{\mathbf{A}}^{\text{sub}} \mathbf{D}$, hence

$$\mathcal{Z} = (\mathbf{A}^{\text{sub}})^{\text{H}} \mathbf{A}^{\text{sub}} = \mathbf{D} \left((\bar{\mathbf{A}}^{\text{sub}})^{\text{H}} \bar{\mathbf{A}}^{\text{sub}} \right) \mathbf{D}. \quad (61)$$

Let $d_{\min} \triangleq \min_i \|\mathbf{a}_i\|_2$. Then

$$\begin{aligned} \lambda_{\min}(\mathcal{Z}) &\geq d_{\min}^2 \lambda_{\min}((\bar{\mathbf{A}}^{\text{sub}})^{\text{H}} \bar{\mathbf{A}}^{\text{sub}}) \\ &\geq d_{\min}^2 (1 - (P-1)\mu_{\text{eff}}). \end{aligned} \quad (62)$$

Equivalently,

$$\frac{\sigma_n^2}{\lambda_{\min}(\mathcal{Z})} \leq \frac{\sigma_n^2}{d_{\min}^2 (1 - (P-1)\mu_{\text{eff}})}. \quad (63)$$

Therefore, a smaller μ_{eff} increases the guaranteed lower bound in (62), thereby tightening (reducing) the conservative upper bound in (63) on the CRLB spectral term $\sigma_n^2 / \lambda_{\min}(\mathcal{Z})$ appearing in (57).

Consequently, imposing the ROI constraint excludes highly coherent columns (e.g., air/background columns), which reduces μ_{eff} and enlarges the guaranteed lower bound on $\lambda_{\min}(\mathcal{Z})$. This tightens the CRLB bound implied by (56)–(63), indicating that ROI-constrained reconstruction can achieve lower attainable estimation error than using the full sensing region.

VI. Numerical Simulations and Results

A. Simulation Setup

In this section, the finite-difference time-domain (FDTD) method is employed to generate EM signals for sensing the scatterers [43]. For simplicity, we assume non-magnetic media and focus on reconstructing the dielectric constitutive parameters, where the unknown contrast χ is fully characterized by the permittivity. The permeability is fixed and not estimated. As illustrated in Fig. 3, a uniform circular antenna array (UCA) of radius 10 m surrounds the sensing region. The simulations use full-wave modeling under the TM_z polarization, yielding a 2-D setting that corresponds to infinitely long z -directed scatterers with cross-sectional permittivity contrast to be reconstructed.

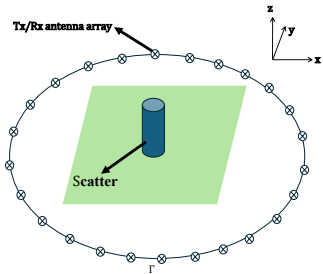


Fig. 3. Schematic diagram of a simplified UCA array.

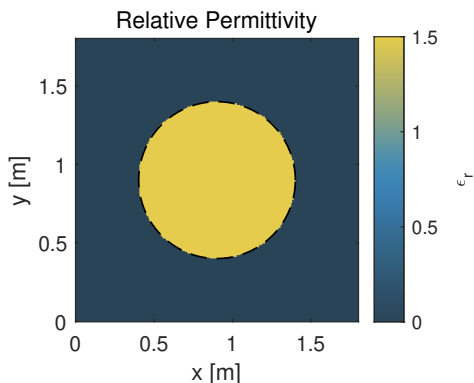


Fig. 4. Geometry of the circular scatterer with a radius of 0.5 m.

The UCA has a radius of 10 m and consists of $N_t = N_r = 60$ antenna elements, uniformly spaced, and used for both transmission and reception.

The center frequency is set to $f_c = 28$ GHz, and frequency spacing $\Delta f = 100$ MHz. We probe $K = 32$ frequencies $\{f_k\}_{k=1}^K$ and allocate $T = 8$ pilot symbols for each frequency to obtain pilot-aided channel observations. The iterative reconstruction process is executed for $M = 10$ iterations.

The sensing region D is uniformly discretized into a 36×36 pixel grid centered at the origin. In all simulations of this section, the parameters used for threshold computation of η are fixed as $\epsilon = 10^{-4}$ and $q_{\text{trim}} = 0.05$. Numerical simulations are conducted using the FDTD method to obtain EM field for four cases of scatterers.

B. Condition Number and Complexity

Fig. 4 illustrates a $1.8 \text{ m} \times 1.8 \text{ m}$ sensing region containing a circular scatterer with a radius of 0.5 m and a permittivity of 1.5. For reproducibility, the ROI sizes used in the simulations are generated deterministically. Let \mathcal{L}_{\min} denote the side length of the smallest square enclosing the scatterer, and let \mathcal{L}_{\max} denote the side length of the entire square sensing region. Given the total number of shrinking steps L , the ROI side length at step o is defined as

$$\mathcal{L}_o = \text{round}\left(\mathcal{L}_{\max} - \frac{o-1}{L-1}(\mathcal{L}_{\max} - \mathcal{L}_{\min})\right), \quad (64)$$

$$o = 1, \dots, L.$$

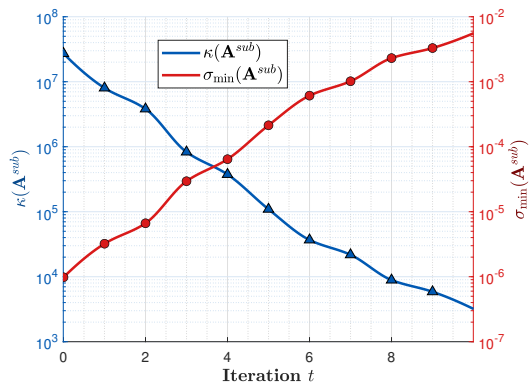


Fig. 5. Variation of the condition number and the smallest singular value.

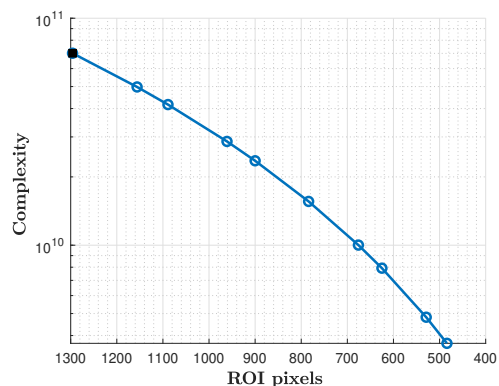


Fig. 6. Computational complexity versus the ROI pixel size.

The corresponding ROI pixel count is then $P_o = \mathcal{L}_o^2$. Hence, once the side length and (\mathcal{L}_{\min}, L) are specified, the ROI sequence is uniquely determined, and the ROI can be iteratively reduced from the full sensing region to progressively smaller square regions enclosing the scatterer.

Fig. 5 illustrates how the condition number and the smallest singular value of \mathbf{A}^{sub} evolve as the ROI size shrinks. At $o = 1$, \mathbf{A}^{sub} coincides with the full-domain operator \mathbf{A} , without any dimensional reduction. In this initial state, the condition number $\kappa(\mathbf{A}^{\text{sub}})$ reaches the order of 10^7 , clearly indicating severe ill-conditioning. Meanwhile, the smallest singular value $\sigma_{\min}(\mathbf{A}^{\text{sub}})$ is only about 10^{-6} , reflecting the rapid decay of the singular value spectrum. From a spectral perspective, this behavior implies that most directions in the solution space are governed by near-null singular modes—primarily contributed by columns corresponding to the air region—thereby amplifying noise and inducing unstable CPR estimates.

As the iterative ROI refinement proceeds, the redundant and highly correlated air-region columns are progressively eliminated. Consequently, the spectral structure of \mathbf{A}^{sub} becomes increasingly dominated by the ASR columns that encode the intrinsic EM features of the scatterer. This selective elimination effectively enhances the effective rank of \mathbf{A}^{sub} , allowing more singular values to retain appreciable magnitudes and thus mitigating the rapid

spectral decay observed in the full-domain case. As a result, the minimum singular value $\sigma_{\min}(\mathbf{A}^{\text{sub}})$ increases from a nearly singular level of 10^{-6} to approximately 10^{-2} , while the condition number $\kappa(\mathbf{A}^{\text{sub}})$ decreases from a severely ill-conditioned 10^7 to a more stable level on the order of 10^3 . This significant spectral improvement verifies that constraining the ROI not only stabilizes the inversion process but also enhances the reliability of CPR reconstruction by suppressing noise-sensitive components.

Fig. 6 illustrates the computational gain achieved by introducing the ROI constraint, which effectively reduces the number of sensing pixels participating in the reconstruction. As the iterations proceed and the ROI becomes progressively refined, the number of pixels inside the ROI decreases from 1,296 (full domain) to 497. Consequently, the algorithmic complexity is reduced by nearly a tenfold factor.

This reduction demonstrates that the ROI constraint not only enhances the numerical conditioning of the forward operator but also provides substantial computational savings by focusing the reconstruction solely on the physically meaningful scatterer region, rather than the redundant air background.

C. CPR Results

To further assess the performance of the proposed method, we present the CPR results for dielectric contrast reconstruction under different scenarios.

Specifically, our comparisons are designed to probe the impact of the scattering operator in the ROI-restricted linear model (7), rather than to establish state-of-the-art performance across different inversion paradigms. To this end, we employ a conventional BIM with Tikhonov regularization as a reference implementation of the linearized update, because its reconstruction behavior is primarily dictated by the conditioning of the associated scattering operator. All methods are evaluated under an identical forward model and the same noise realization, and they share the same ROI mask (obtained by the same procedure). Moreover, the regularization parameters in both methods are selected by the same L-curve criterion. Unless otherwise specified, both methods are run for 10 outer iterations. The remaining simulation parameters follow Subsection VI-A.

1) Single Scatterer (Triangular Case): The permittivity for triangle case is set to 2. Fig. 7(a) depicts an equilateral triangular scatterer with an area of 0.65 m^2 . We first apply the LSM under 5 dB noise with the regularization parameter $\zeta = 10^{-3}$. After thresholding, the ROI shown in Fig. 7(b) is extracted, which reduces the problem dimension from 1,296 to 426 pixels. Within this ROI, we run the ROI-constrained QP under both 5 dB and 30 dB signal-to-noise ratios (SNRs), as shown in Figs. 7(c) and 7(d), respectively. In both cases, the proposed ROI-QP successfully recovers the scatterer geometry, while a higher SNR further improves the accuracy of the reconstructed internal permittivity. For comparison, Figs. 7(e)

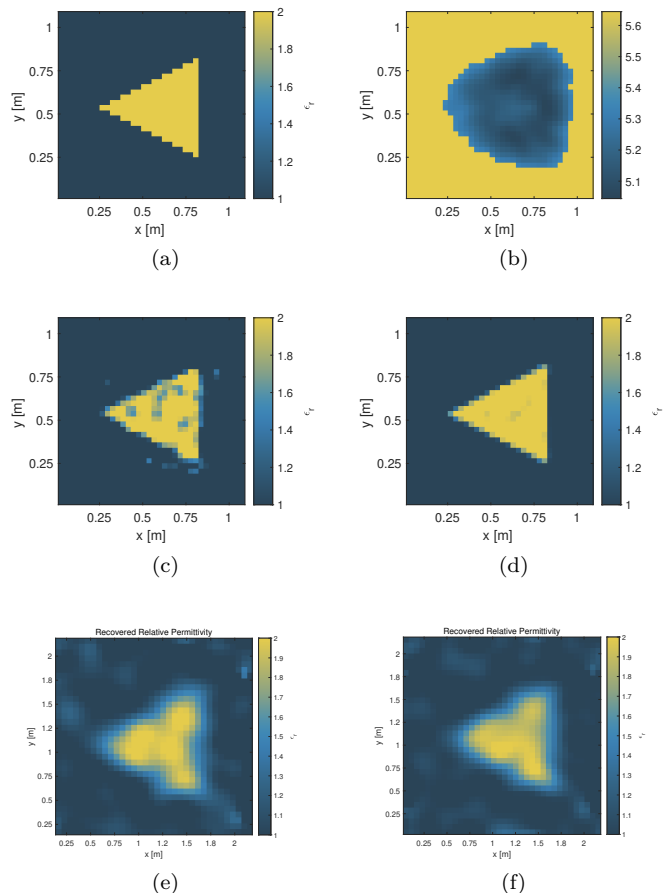


Fig. 7. (a) True permittivity; (b) ROI obtained after truncation; (c)–(d) ROI-QP reconstructions (single-step Born linearization) at 5 and 30 dB; (e)–(f) BIM reconstructions at 5 and 30 dB.

and 7(f) report results generated by the baseline. We observe that, under the same simulation setting, ROI-constrained QP achieves more accurate CPR results.

2) Non-convex scatterer (T-shape): We investigate the impact of the ROI constraint on the CPR performance in the presence of a non-convex scatterer under 5 dB SNR. We consider a T-shaped target with arm length of 1.1 m of both axis, a width of 0.24 m, and a permittivity of 1.5. All other parameters are kept the same as those in the previous subsection. Figs. 8(a) and 8(b) show the ground-truth permittivity distribution and the ROI delineated by the LSM (with $\zeta = 10^{-4}$), respectively. Figs. 8(c) and 8(d), as well as Figs. 8(e) and 8(f), present the CPR results of QP and BIM under the full-domain setting and the ROI-constrained setting, respectively. It can be observed that QP with the ROI constraint yields a noticeably improved reconstruction compared with its full-domain counterpart. For BIM, both reconstructions appear blurred relative to the ground truth; nevertheless, the ROI-constrained BIM produces less severe artifacts around the geometric boundary of the T-shaped target, indicating improved robustness. Overall, this simulation demonstrates that imposing an ROI constraint helps alleviate the ill-conditioning and lead to a better CPR

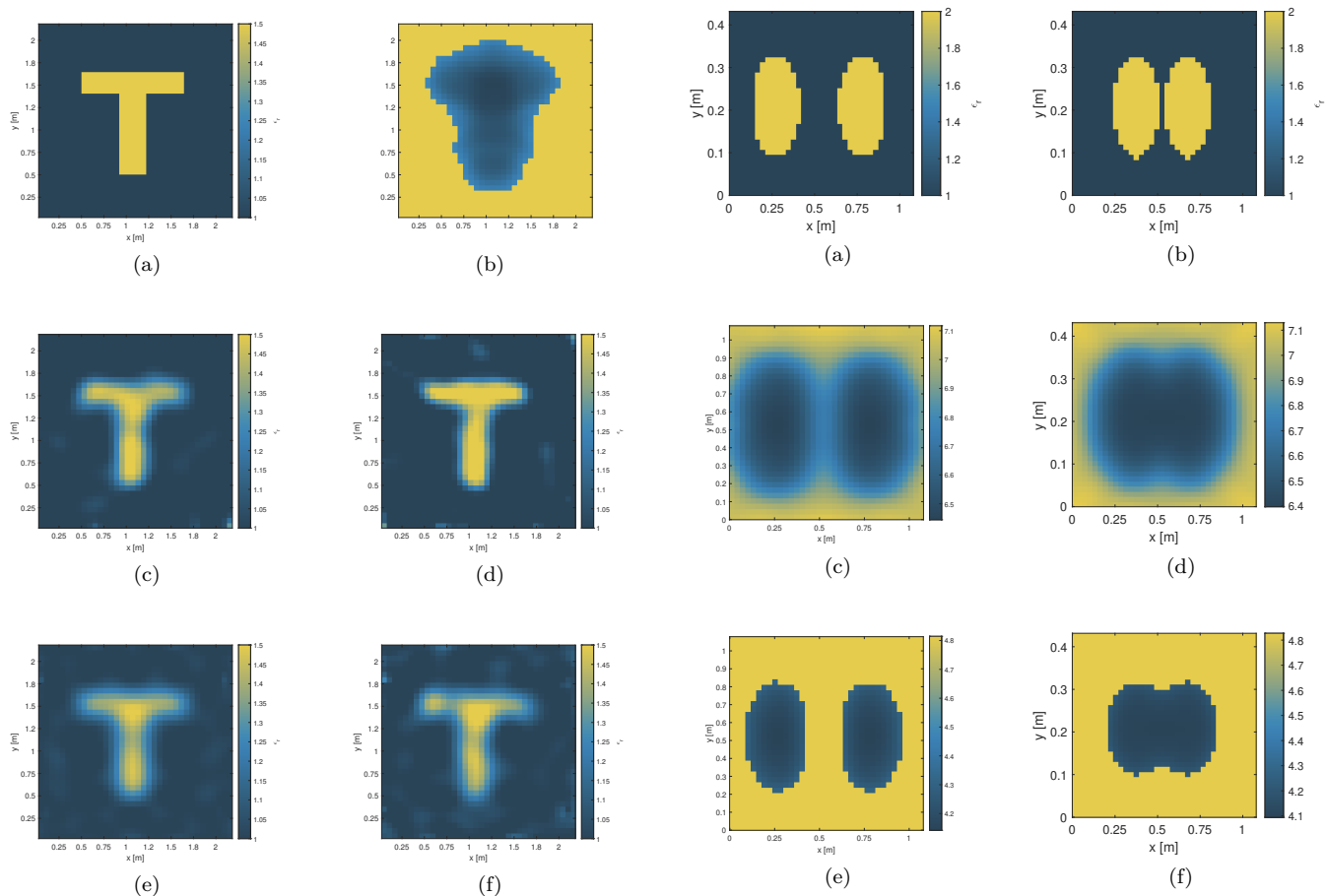


Fig. 8. (a) True permittivity; (b) ROI obtained after truncation; (c)–(d) QP under the full-domain case and the ROI-constrained case at 5 dB SNR; (e)–(f) BIM under the full-domain case and the ROI-constrained case at 5 dB SNR.

performance.

3) Multiple Scatterers (Elliptical Cluster Case): Next, we evaluate the performance of the ROI-QP scheme for a cluster of two closely spaced elliptical scatterers. The scatterers have relative permittivity 2, and the SNR is set to 5 dB. Each ellipse has a major axis of 0.12 m and a minor axis of 0.055 m, and the center-to-center spacing is set to 0.3 m and 0.1 m, respectively.

The corresponding geometric reconstructions obtained by the LSM (with $\zeta = 10^{-4}$) are presented in Figs. 9(a) and 9(e). When applied to a cluster of scatterers, the LSM exhibits a noticeable “sticking” effect along the boundaries of adjacent objects. This phenomenon arises because the LSM inherently produces spatially extended high-response regions surrounding strong permittivity boundaries. As the separation between scatterers approaches the resolution limit of the sensing aperture, these regions overlap and merge, resulting in apparent boundary adhesion and a loss of distinct object separation. After applying a suitable threshold to suppress weak responses, the ROIs corresponding to the two spacing cases are obtained, as shown in Figs. 9(c) and 9(g). For the 0.3 m spacing, the ROI successfully encloses both ellipses within a moder-

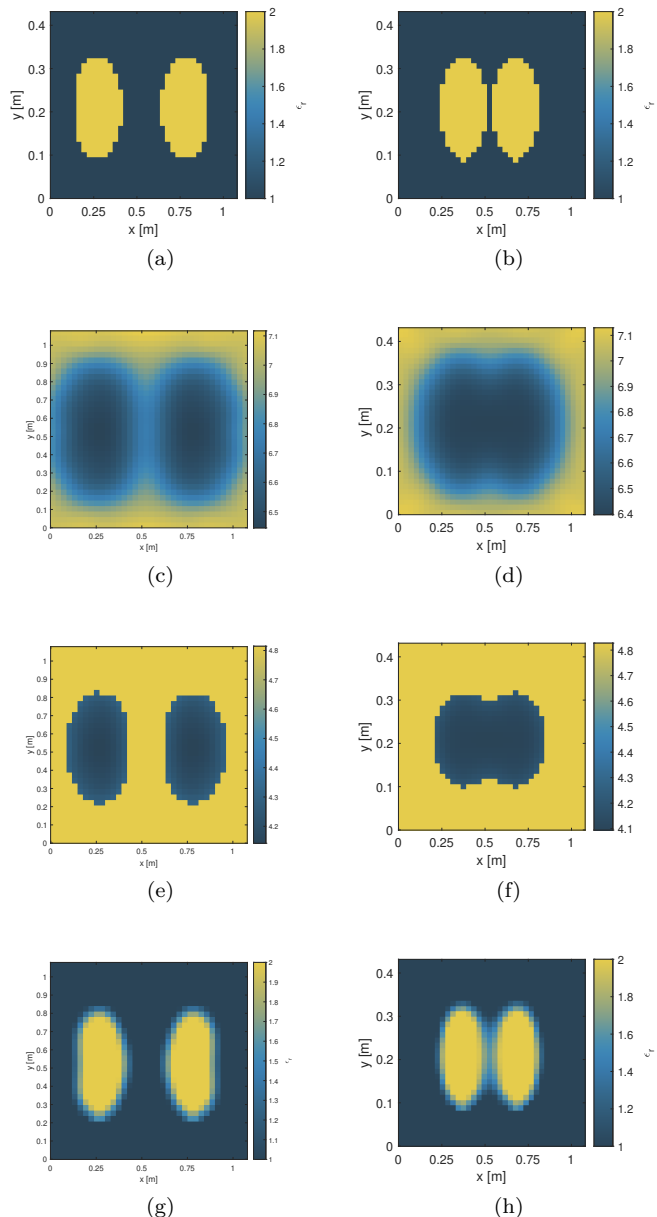
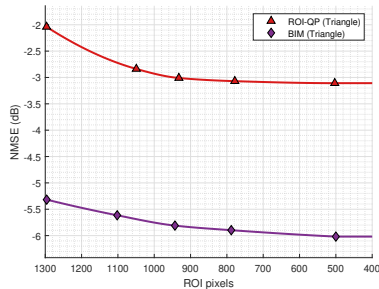


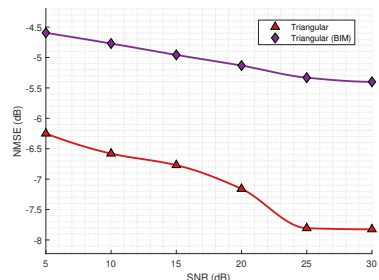
Fig. 9. (a)–(d) Case with 0.3 m spacing: (a) true permittivity, (b) LSM sensing, (c) truncated ROI, and (d) ROI-QP reconstruction at 10 dB. (e)–(h) Case with 0.1 m spacing: (e) true permittivity, (f) LSM sensing, (g) truncated ROI, and (h) ROI-QP reconstruction at 10 dB.

ately expanded boundary, providing accurate geometric localization. In contrast, for the 0.1 m spacing, the ROI can no longer fully resolve the two ellipses, and partial adhesion occurs between their boundaries.

Performing ROI-QP, the results presented in Figs. 9(d) and 9(h) show that the proposed method accurately recovers both the shape and permittivity values of the scatterers for both inter-scatterer spacings, with only minor artifacts appearing near the boundaries. Even when the LSM-derived ROI suffers from boundary adhesion at 0.1 m spacing, this issue is largely alleviated during the ROI-QP refinement. This improvement stems from the data-consistency enforcement inherent in the Born iter-



(a)



(b)

Fig. 10. NMSE results for the triangular scatterer: (a) NMSE versus ROI pixels, and (b) NMSE versus SNR.

ation, which continuously adjusts the reconstructed permittivity to minimize the residual between the simulated and measured scattering fields. Through this feedback mechanism, the algorithm adaptively distinguishes subtle dielectric variations between the closely spaced scatterers, thereby restoring their individual shapes and improving the reconstruction fidelity.

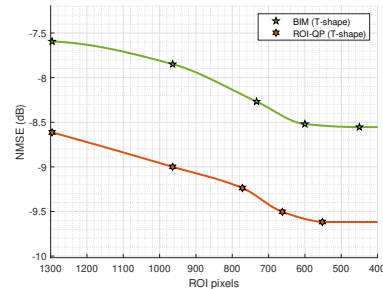
Overall, these results highlight that the proposed ROI-QP approach maintains robust separation capability and stable permittivity recovery even in highly coupled, relatively low-SNR environments, where traditional qualitative methods such as the LSM alone tend to fail.

D. Normalized Mean Square Error Analysis

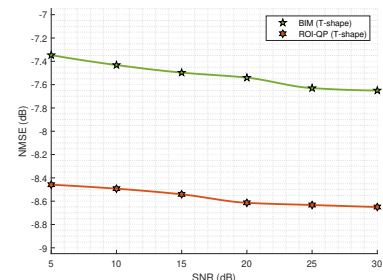
In this subsection, we validate the above conclusions by examining how the normalized mean square error (NMSE) of all CPR simulation results varies with the ROI size and the noise level (in dB); see Figs. 10–12. In particular, when investigating the NMSE–ROI-pixel trend, we fix the number of QP iterations to one (i.e., a single Born step) to control for any additional performance gain introduced by the QP refinement itself, so that the observed variation mainly reflects the improvement brought by the ROI constraint. In contrast, for the NMSE–SNR results, the QP refinement is executed with the nominal iteration setting to report the performance of the full reconstruction pipeline. The NMSE of χ , expressed in dB, is defined as

$$\text{NMSE} = 10 \log_{10} \left(\frac{\|\hat{\chi} - \chi\|_2^2}{\|\chi\|_2^2} \right). \quad (65)$$

From Figs. 10(a) and 11(a), we observe that, at SNR = 30 dB, the NMSE of both ROI-QP and Tikhonov-BIM decreases as the ROI shrinks from the full domain (1,296

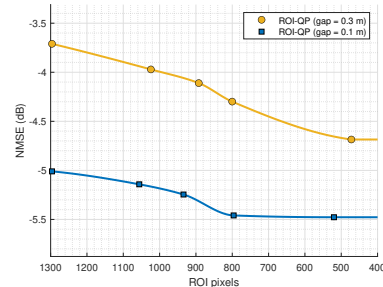


(a)

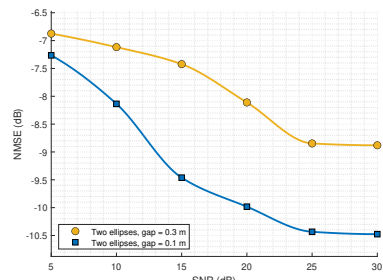


(b)

Fig. 11. NMSE results for the T-shaped scatterer: (a) NMSE versus ROI pixels, and (b) NMSE versus SNR.



(a)



(b)

Fig. 12. NMSE results for the two-ellipse cases: (a) NMSE versus ROI pixels, and (b) NMSE versus SNR.

pixels) toward the ASR, confirming the benefit of removing redundant background pixels. The NMSE reduction is about 1 dB for ROI-QP (triangular and T-shape) and for Tikhonov-BIM (T-shape), while the triangular case with Tikhonov-BIM improves by about 0.7 dB. Note that the NMSE–ROI curves are obtained with a single QP iteration (one-step Born update) to exclude the gain from iterative

refinement; consequently, ROI-QP appears roughly 3 dB worse than Tikhonov-BIM in this controlled setting.

When the nominal iterations are enabled, as shown in Figs. 10(b) and 11(b), ROI-QP achieves higher accuracy, and both methods exhibit the expected monotonic NMSE decrease with increasing SNR. A similar decreasing trend with respect to the ROI size is also observed for the two-ellipse cases in Fig. 12(a), and the corresponding NMSE–SNR behavior is reported in Fig. 12(b), where the smaller gap (0.1 m) yields a lower initial NMSE and a milder sensitivity to ROI reduction.

In summary, the NMSE trends of both ROI-QP and BIM with respect to the ROI pixel number corroborate our theoretical analysis. Moreover, under the nominal iteration setting, ROI-QP achieves improved reconstruction accuracy across different scatterer geometries and noise conditions.

VII. Conclusion

This paper has investigated the fundamental origins of ill-conditioning in CSI-based EM material reconstruction in ISAC systems. From an operator-centric viewpoint, we reveal a spectral dichotomy in the resulting ISAC scattering operator: background-related columns are highly coherent and drive near rank deficiency, whereas scatterer-related columns are comparatively weakly correlated and govern the effective rank. These findings provide a physics-grounded justification for ROI-restricted inversion as a principled way to stabilize the inverse problem. To quantify the benefit of subspace restriction, we derive analytical bounds on the condition-number reduction and establish the associated tightening of the CRLB. Guided by these insights, we implement an ROI-constrained QP framework with LSM-based ROI initialization. Full-wave FDTD simulations validate that the gains in robustness and reconstruction accuracy stem from the identified operator structure—rather than from heuristic algorithmic tuning. Overall, this work lays a theoretical foundation for material-aware digital twins enabled by future ISAC networks.

Appendix A

The Required Khatri-Rao Identity

For any vectors $\mathbf{x}, \mathbf{z} \in \mathbb{C}^m$ and $\mathbf{y}, \mathbf{w} \in \mathbb{C}^n$, the following identities hold:

$$(\mathbf{x} \circ \mathbf{y})^H (\mathbf{z} \circ \mathbf{w}) = (\mathbf{x}^H \mathbf{z}) (\mathbf{y}^H \mathbf{w}), \quad (\text{A.1})$$

$$\|\mathbf{x} \circ \mathbf{y}\|_2 = \|\mathbf{x}\|_2 \|\mathbf{y}\|_2. \quad (\text{A.2})$$

Appendix B

Air-Region Column Coherence—Continued

For notational simplicity, we fix a tone k and omit the subscript k in this appendix. Under an (approximately) wide-sense stationary (WSS) propagation model, channel responses observed at two nearby spatial locations

are locally coherent: their second-order statistics depend primarily on the displacement $\Delta r = r_j - r_i$, and the normalized spatial correlation remains close to one when $\|\Delta r\|$ lies within the coherence distance. As a result, the sub-vectors \mathbf{u}_j and \mathbf{v}_j associated with air-region pixels are nearly colinear with \mathbf{u}_i and \mathbf{v}_i , respectively. We formalize this near-colinearity by the following scaling-plus-residual relations:

$$\begin{aligned} \mathbf{u}_j &= \gamma_{ij} \mathbf{u}_i + \Delta \mathbf{u}, & \|\Delta \mathbf{u}\|_2 &\leq \varepsilon_u \|\mathbf{u}_i\|_2, \\ \mathbf{v}_j &= \rho_{ij} \mathbf{v}_i + \Delta \mathbf{v}, & \|\Delta \mathbf{v}\|_2 &\leq \varepsilon_v \|\mathbf{v}_i\|_2. \end{aligned} \quad (\text{B.1})$$

Here, $\gamma_{ij}, \rho_{ij} \in \mathbb{C}$ denote the best complex scalings (projections), while $\varepsilon_u, \varepsilon_v \ll 1$ quantify the local decoherence induced by the spatial displacement.

Define

$$\begin{aligned} U &\triangleq \|\mathbf{u}_i\|_2, \\ V &\triangleq \|\mathbf{v}_i\|_2, \\ \delta_{ij} &\triangleq |\gamma_{ij}| \varepsilon_v + |\rho_{ij}| \varepsilon_u + \varepsilon_u \varepsilon_v. \end{aligned} \quad (\text{B.2})$$

We compute the (i, j) -th entry of the Gram matrix of \mathbf{A} . By the Khatri–Rao property (A.1),

$$\langle \mathbf{a}_i, \mathbf{a}_j \rangle = (\mathbf{u}_i^H \mathbf{u}_j) (\mathbf{v}_i^H \mathbf{v}_j). \quad (\text{B.3})$$

Substituting (B.1) into (B.3) gives

$$\begin{aligned} \mathbf{u}_i^H \mathbf{u}_j &= \gamma_{ij} \|\mathbf{u}_i\|_2^2 + \mathbf{u}_i^H \Delta \mathbf{u}, \\ \mathbf{v}_i^H \mathbf{v}_j &= \rho_{ij} \|\mathbf{v}_i\|_2^2 + \mathbf{v}_i^H \Delta \mathbf{v}. \end{aligned} \quad (\text{B.4})$$

By the Cauchy–Schwarz inequality and (B.1),

$$\begin{aligned} |\mathbf{u}_i^H \Delta \mathbf{u}| &\leq \|\mathbf{u}_i\|_2 \|\Delta \mathbf{u}\|_2 \leq \varepsilon_u U^2, \\ |\mathbf{v}_i^H \Delta \mathbf{v}| &\leq \|\mathbf{v}_i\|_2 \|\Delta \mathbf{v}\|_2 \leq \varepsilon_v V^2. \end{aligned} \quad (\text{B.5})$$

Combining the expansion of (B.3) with triangle inequality and the bounds in (B.5), we obtain

$$|\langle \mathbf{a}_i, \mathbf{a}_j \rangle| \geq (|\rho_{ij} \gamma_{ij}| - \delta_{ij}) U^2 V^2, \quad (\text{B.6})$$

where δ_{ij} is defined in (B.2).

From property (A.2),

$$\|\mathbf{a}_i\|_2 = \|\mathbf{u}_i\|_2 \|\mathbf{v}_i\|_2 = UV, \quad \|\mathbf{a}_j\|_2 = \|\mathbf{u}_j\|_2 \|\mathbf{v}_j\|_2. \quad (\text{B.7})$$

Moreover, by (B.1) and triangle inequality,

$$\|\mathbf{u}_j\|_2 \leq (|\gamma_{ij}| + \varepsilon_u)U, \quad \|\mathbf{v}_j\|_2 \leq (|\rho_{ij}| + \varepsilon_v)V, \quad (\text{B.8})$$

hence

$$\|\mathbf{a}_j\|_2 \leq (|\gamma_{ij}| + \varepsilon_u)(|\rho_{ij}| + \varepsilon_v)UV. \quad (\text{B.9})$$

The NCC between the two columns is

$$\mu_{ij} \triangleq \frac{|\langle \mathbf{a}_i, \mathbf{a}_j \rangle|}{\|\mathbf{a}_i\|_2 \|\mathbf{a}_j\|_2}, \quad (\text{B.10})$$

and combining (B.6)–(B.10) yields

$$\mu_{ij} \geq \frac{|\rho_{ij} \gamma_{ij}| - \delta_{ij}}{(|\gamma_{ij}| + \varepsilon_u)(|\rho_{ij}| + \varepsilon_v)}. \quad (\text{B.11})$$

For air-region pixels within a reasonably sized sensing region D , the large-scale fading changes slowly over small displacements, while the small-scale fading remains locally coherent due to limited angular spread. Consequently, when $\|\Delta r\|$ is within the coherence distance, the residuals in (B.1) are small:

$$\varepsilon_u(\Delta r) \ll 1, \quad \varepsilon_v(\Delta r) \ll 1. \quad (\text{B.12})$$

Moreover, $|\gamma_{ij}|$ and $|\rho_{ij}|$ stay uniformly bounded away from zero in this locally coherent regime, so the denomi-

nator of (B.11) is a bounded $\mathcal{O}(1)$ factor. Therefore, (B.11) can be simplified to

$$\mu_{ij} \geq 1 - C\delta_{ij}, \quad (\text{B.13})$$

where $C = \mathcal{O}(1)$ is a constant. Hence, μ_{ij} is close to 1 for any two air-region columns, implying strong inter-column coherence and, consequently, severe ill-conditioning of the full-domain operator.

References

- [1] F. Liu, Y. Cui, C. Masouros, et al., "Integrated sensing and communications: Toward dual-functional wireless networks for 6G and beyond," *IEEE J. Sel. Areas Commun.*, vol. 40, no. 6, pp. 1728–1767, Jun. 2022.
- [2] Y. Zhang, J. Zhang, H. Gong, et al., "A unified RCS modeling of typical targets for 3GPP ISAC channel standardization and experimental analysis," *IEEE J. Sel. Areas Commun.*, 2025.
- [3] Y. Xiong, F. Liu, Y. Cui, et al., "On the fundamental tradeoff of integrated sensing and communications under Gaussian channels," *IEEE Trans. Inf. Theory*, vol. 69, no. 9, pp. 5723–5751, Sep. 2023.
- [4] J. Wang, J. Zhang, Y. Zhang, et al., "Radio environment knowledge pool for 6G digital twin channel," *IEEE Commun. Mag.*, vol. 63, no. 5, pp. 158–164, May 2025.
- [5] Y. Luo, L. Yu, Y. Miao, et al., "An adaptive shooting and bouncing rays method for ray-tracing channel modeling assisted by environmental prior information for 6G," in *Proc. IEEE PIMRC, Valencia, Spain, 2024*.
- [6] A. Bazzi, M. Ying, O. Kanhere, T. S. Rappaport and M. Chafii, "ISAC Imaging by Channel State Information Using Ray Tracing for Next Generation 6G", *IEEE J. Sel. Topics Electromagnetics Antennas Propag.*, vol. 1, no. 1, pp. 135–149, Sept. 2025.
- [7] J. Zhang, J. Lin, P. Miao, et al., "Deterministic ray tracing: A promising approach to THz channel modeling in 6G deployment scenarios," *IEEE Commun. Mag.*, vol. 62, no. 2, pp. 48–54, Feb. 2024.
- [8] P. Li, Y. Shao, and R. Xu, "Complex permittivity extraction of typical wooden furniture materials based on multi-objective particle swarm optimization over 40–50 GHz," in *Proc. EuCAP, Glasgow, U.K., 2024*.
- [9] A. Diepolder, M. Mueh, S. Brandl, et al., "A novel rotation-based standardless calibration and characterization technique for free-space measurements of dielectric material," *IEEE J. Microwaves*, vol. 4, no. 1, pp. 56–68, Jan. 2024.
- [10] H. Zhou, H. Chen, J. Yang, et al., "Improvement of permittivity measurement for materials with arbitrary thickness based on rectangular waveguide," *IEEE Trans. Instrum. Meas.*, 2025.
- [11] S. Mao, M. Ji, B. Wang, et al., "Surface material perception through multimodal learning," *IEEE J. Sel. Topics Signal Process.*, vol. 16, no. 4, pp. 843–853, Jun. 2022.
- [12] H. Liu, F. Sun, and X. Zhang, "Robotic material perception using active multimodal fusion," *IEEE Trans. Ind. Electron.*, vol. 66, no. 12, pp. 9489–9499, Dec. 2019.
- [13] G. Schwartz and K. Nishino, "Recognizing material properties from images," *IEEE Trans. Pattern Anal. Mach. Intell.*, vol. 42, no. 8, pp. 1981–1995, Aug. 2020.
- [14] A. Zakutayev, N. Wunder, M. Schwarting, et al., "An open experimental database for exploring inorganic materials," *Sci. Data*, vol. 5, no. 1, p. 180053, Apr. 2018.
- [15] X. Huang, W. Qian, J. Liu, et al., "EM database v1.0: A benchmark informatics platform for data-driven discovery of energetic materials," *Energ. Mater. Front.*, vol. 5, no. 4, pp. 267–273, Dec. 2024.
- [16] V. Gupta, W.-k. Liao, A. Choudhary, et al., "Combining transfer learning and representation learning to improve predictive analytics on small materials data," in *Proc. ICMLA, Miami, FL, USA, 2024*.
- [17] D. Colton and R. Kress, *Inverse Acoustic and Electromagnetic Scattering Theory*, 3rd ed. New York: Springer, 1998.
- [18] J. O. Vargas and R. Adriano, "Subspace-based conjugate-gradient method for solving inverse scattering problems," *IEEE Trans. Antennas Propag.*, vol. 70, no. 12, pp. 12139–12146, Dec. 2022.
- [19] X. Huang, "Integral equation methods with multiple scattering and Gaussian beams in inhomogeneous background media for solving nonlinear inverse scattering problems," *IEEE Trans. Geosci. Remote Sens.*, vol. 59, no. 6, pp. 5345–5351, Jun. 2021.
- [20] Y. Luo, L. Yu, T. Wu, et al., "A robust CSI-based scatterer geometric reconstruction method for 6G ISAC system," *arXiv preprint arXiv:2510.16389*, 2025.
- [21] Y. Jiang, F. Gao, and S. Jin, "Electromagnetic property sensing: A new paradigm of integrated sensing and communication," *IEEE Trans. Wireless Commun.*, vol. 23, no. 10, pp. 13471–13483, Oct. 2024.
- [22] Y. Jiang, F. Gao, S. Jin, et al., "Electromagnetic property sensing in ISAC with multiple base stations: Algorithm, pilot design, and performance analysis," *IEEE Trans. Wireless Commun.*, vol. 24, no. 4, pp. 3400–3416, Apr. 2025.
- [23] L. Wen, S. Zhao, T. Yin, Y. Guo and X. Chen, "Inverse Scattering Approach to Integration of Communication and Sensing", *IEEE J. Sel. Topics Electromagnetics Antennas Propag.*, vol. 1, no. 1, pp. 20–36, 2025.
- [24] A. N. Tikhonov and V. Y. Arsenin, *Solutions of Ill-Posed Problems*. Washington, DC: Winston, 1977.
- [25] M. Brekke and M. Hanke, *Regularization of Inverse Problems*. Dordrecht: Kluwer, 1999.
- [26] T. Søndergaard and B. Tromborg, "Lippmann–Schwinger integral equation approach to the emission of radiation by sources located inside finite-sized dielectric structures," *Phys. Rev. B*, vol. 66, no. 15, p. 155313, Oct. 2002.
- [27] T.-a. Pham, E. Soubies, A. Ayoub, et al., "Three-dimensional optical diffraction tomography with Lippmann–Schwinger model," *IEEE Trans. Comput. Imag.*, vol. 6, pp. 727–738, 2020.
- [28] F. Wang and Q. Liu, "A hybrid Born iterative Bayesian inversion method for electromagnetic imaging of moderate-contrast scatterers with piecewise homogeneities," *IEEE Trans. Antennas Propag.*, vol. 70, no. 10, pp. 9652–9661, 2022.
- [29] F. Wang, K. Li, Y. Mao, and Q. Liu, "A hybrid Born iterative method for diagnosis of planar arrays with amplitude-only far-field measurements," *IEEE Antennas Wireless Propag. Lett.*, vol. 23, no. 2, pp. 548–552, Feb. 2024.
- [30] D. Liu, T. Shan, M. Li, et al., "Multi-frequency neural Born iterative method for solving 2-D inverse scattering problems," *IEEE Trans. Comput. Imag.*, vol. 11, pp. 1243–1257, 2025.
- [31] R. F. Harrington, *Time-Harmonic Electromagnetic Fields*. New York: McGraw-Hill, 1961.
- [32] A. Costa Batista, R. Adriano, and L. S. Batista, "EISPY2D: An open-source Python library for the development and comparison of algorithms in two-dimensional electromagnetic inverse scattering problems," *IEEE Access*, vol. 13, pp. 92134–92154, 2025.
- [33] S. J. Ziegler and M. J. Burfeindt, "Frequency beamforming-enhanced DBIM for limited-aperture quantitative imaging," *IEEE Trans. Antennas Propag.*, vol. 73, no. 2, pp. 1173–1184, Feb. 2025.
- [34] J. Geiss, E. Sippel, M. Braunwarth, and M. Vossiek, "The Impact of Antenna Array Calibration Errors on MIMO and Multi-Channel Synthetic Aperture Radar Imaging," *IEEE J. Microw.*, vol. 3, no. 2, pp. 635–654, Apr. 2023.
- [35] H. Hoang, M. John, P. McEvoy, and M. J. Ammann, "Calibration to Mitigate Near-Field Antennas Effects for a MIMO Radar Imaging System," *Sensors*, vol. 21, no. 2, Art. no. 514, Jan. 2021.
- [36] Z. Zhao, W. Tian, Y. Deng, C. Hu, and T. Zeng, "Calibration Method of Array Errors for Wideband MIMO Imaging Radar Based on Multiple Prominent Targets," *Remote Sens.*, vol. 13, no. 15, Art. no. 2997, Jul. 2021.
- [37] J. Garnier, H. Haddar, and H. Montanelli, "The linear sampling method for random sources," *SIAM J. Imag. Sci.*, vol. 16, no. 3, pp. 1572–1593, 2023.
- [38] A. Pizzo, T. L. Marzetta, and L. Sanguinetti, "Spatially-stationary model for holographic MIMO small-scale fading," *IEEE J. Sel. Areas Commun.*, vol. 38, no. 9, pp. 1964–1979, Sep. 2020.
- [39] 3GPP, "Study on channel model for frequencies from 0.5 to 100 GHz," 3GPP TR 38.901, v16.1.0 (Release 16), Nov. 2020.
- [40] L. Crocco, I. Catapano, L. Di Donato, et al., "The linear sampling method as a way to quantitative inverse scattering," *IEEE Trans. Antennas Propag.*, vol. 60, no. 4, pp. 1844–1853, Apr. 2012.

- [41] P. Monk, M. Pena, and V. Selgas, "Multifrequency linear sampling method on experimental datasets," *IEEE Trans. Antennas Propag.*, vol. 71, no. 11, pp. 8788–8798, Nov. 2023.
- [42] A. K. Cline, C. B. Moler, G. W. Stewart, et al., "An estimate for the condition number of a matrix," *SIAM J. Numer. Anal.*, vol. 16, no. 2, pp. 368–375, Apr. 1979.
- [43] A. Costa Batista, L. S. Batista, and R. Adriano, "A quadratic programming approach for microwave imaging," *IEEE Trans. Antennas Propag.*, vol. 69, no. 8, pp. 4923–4934, Aug. 2021.
- [44] M. Pirani and S. Sundaram, "On the smallest eigenvalue of grounded Laplacian matrices," *IEEE Trans. Autom. Control*, vol. 61, no. 2, pp. 509–514, Feb. 2016.
- [45] Gurobi Optimization, "Gurobi optimizer reference manual," 2019. [Online]. Available: <http://www.gurobi.com>
- [46] F. Liu and C. Masouros, "Hybrid beamforming with sub-arrayed MIMO radar: Enabling joint sensing and communication at mmWave band," in *Proc. ICASSP*, Brighton, U.K., 2019, pp. 2517–2521.
- [47] H. N. Salas, "Gershgorin's theorem for matrices of operators," *Linear Algebra Appl.*, vol. 291, pp. 15–36, Apr. 1999.
- [48] M. Brignone, J. Coyle, and M. Piana, "The use of the linear sampling method for obtaining super-resolution effects in Born approximation," *J. Comput. Appl. Math.*, vol. 203, no. 1, pp. 145–158, 2007.